

Tel Aviv University
Raymond and Beverly Sackler
Faculty of Exact Sciences

Prospects for Kaluza-Klein Excitations Search in the Di-Lepton Channel at the LHC

This thesis is submitted towards the M.Sc. degree

At Tel Aviv University
The Raymond and Beverly Sackler School of
Physics and Astronomy

By
Evgeny Yurkovsky

Under the Supervision of
Prof. Erez Etzion and Prof. Yaron Oz

February 3, 2009

Abstract

Based on the Kaluza-Klein (KK) theory and extra heavy boson models, we have studied the possibility to explore the consequences of those theories at the LHC experiments.

We focused on KK excitations of $SU(2) \times U(1)$ gauge fields in extra dimensions when the fermions and the $SU(3)$ gauge Bosons are localized in the 3d brane. Alternatively, we consider the possibility of existence of an extra heavy boson Z' coming from breaking the E_6 groups.

By looking at the di-lepton invariant mass and the forward-backward asymmetry of the neutral Drell-Yan process $pp \rightarrow l^+l^- X$ we studied the differences between Z^* (KK Z^0 excitations) and Z' . We calculated the upper limits of resonance mass which can be discovered or excluded at the LHC with integrated luminosity of 10fb^{-1} , expected for the first year of LHC operation. In addition, we studied the sensitivity of various methods to distinguish between Z^* and Z' and between different Z' models.

Contents

| | | |
|----------|--|-----------|
| 1 | Introduction | 3 |
| 2 | Theoretical Framework | 5 |
| 2.1 | Kaluza-Klein Excitations | 7 |
| 2.2 | Extra Heavy Boson | 8 |
| 3 | The Large Hadron Collider | 10 |
| 3.1 | ATLAS Detector | 13 |
| 4 | Expected Sensitivity at the LHC | 17 |
| 4.1 | Di-Lepton Invariant Mass | 20 |
| 4.2 | Forward-Backward Asymmetry | 27 |
| 4.3 | Invisible Resonance | 33 |
| 5 | Monte Carlo Generator | 37 |
| 5.1 | Invariant Mass Distribution | 38 |
| 5.2 | Forward-Backward Asymmetry | 40 |
| 6 | Summary and Conclusions | 44 |
| A | Appendix - Kaluza-Klein Theory | 47 |

1 Introduction

The Large Hadron Collider (LHC) will begin operation this year and will test some intriguing suggestions for what might lie beyond the standard model (SM) of particle physics. One of the most surprising ideas centers on the possible existence of extra dimensions of space [1].

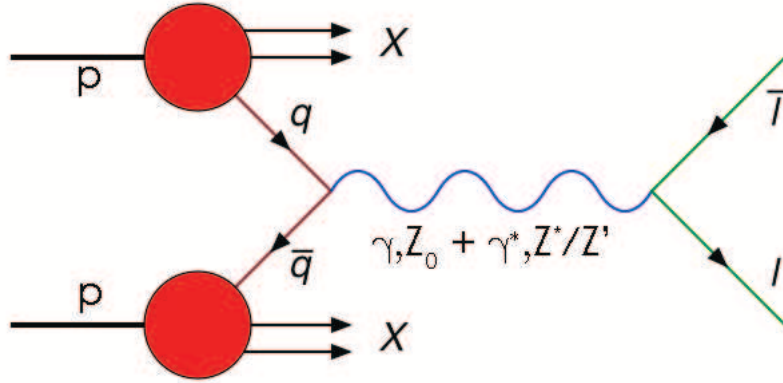


Figure 1: Neutral Drell-Yan process $pp \rightarrow l^+l^-X$ with additional gauge fields.

In our study we focused on the Kaluza-Klein (KK) excitations of $SU(2) \times U(1)$ gauge fields in extra dimension, where the fermions and the $SU(3)$ gauge bosons are localized in three regular spacial dimensions (3d brane). We further studied the signature of an extra heavy boson coming from breaking the E_6 groups and compared the two models with respect to the SM.

By looking at the leading order (LO) modified cross section of the neutral Drell-Yan process $pp \rightarrow l^+l^-X$ (Fig. 1), which consist of SM and New Physics (NP) parts, one can see the differences between those models. In order to quantify our sensitivity to deviation from the SM, the contribution of New Physics signal is studied. To examine that, we inserted a Breit-Wigner resonance into the SM distribution. Then compared it with generated Monte Carlo data using a binned likelihood method with Poisson statistics. By that we studied the LHC potential reach for detecting

NP signal in this process. This upper limit was compared with the expected visible cross sections for KK model and the various Z' models mentioned above. We derived the mass limits for discovery and exclusion of new possible particles of that type in the LHC.

An alternative method to quantify the sensitivity of LHC to New Physics is to study the angular decay asymmetry and its dependence on the resonance mass. We calculated the forward-backward asymmetry with respect to the boost direction, for a KK excitation and different Z' models. One can see a discrepancy between KK excitations, which behave similar to the SM asymmetry and the Z' models, which are very different.

Using that information, both the cross section and the forward-backward asymmetry, we analyzed the sensitivity to distinguish between extra dimension and unified extra symmetry models.

This work is organized as follows: In the second section we introduced the theoretical framework of extra dimensions as a solution to the hierarchy problem, realization type I string theory with D-brane, Kaluza-Klein excitations of gauge bosons and models of extra heavy Z boson. The third section contains a brief introduction to the Large Hadron Collider and the ATLAS experiment. In the fourth section we describe the main subject of our work - expected sensitivity for NP discovery at the LHC. The fifth section describes a MC simulation of the neutral Drell-Yan process with additional gauge fields. The last, sixth section gives our summary and conclusions. Appendix A describes the mechanism of KK excitations.

2 Theoretical Framework

Most physicists agree that some forms of NP must exist beyond the SM. One possibility is that extra spatial dimensions will begin to show themselves at or near the TeV scale. The study of the physics of TeV scale extra dimensions that has taken place over the past few years has its origins in the ground breaking work of Arkani-Hamed, Dimopoulos and Dvali(ADD) [3]. A wide range of issues have been considered in the extra dimensions context, some of them are:

- hierarchy problem - why gravity appears to us so weak compared to the other three known fundamental interactions corresponding to the electromagnetic, weak and strong nuclear forces [3] [4].
- producing electroweak symmetry breaking without a Higgs boson [5].
- new dark matter candidates and a new cosmological perspective [6].
- black hole production at collider [7].

It is clear from this list that extra dimensions ideas have found their way into essentially every area of interest in high energy physics which certainly makes them worthy of detailed study.

ADD propose that the Planck scale $M_{Pl} \sim G_N^{-1/2}$ is not a fundamental scale; its enormity is simply a consequence of the large size of the new dimensions. The only fundamental short distance scale in nature is the m_{EW} . In that framework all the SM fields must be localized to a 4-dimensional manifold while the gravitons can freely propagate in the new $(4 + n)$ dimensions of radius R . However, there is another possibility. Assume there are n extra dimensions but let $n - p$ of them have a radius R_{\perp} and p of them radius R_{\parallel} ($R_{\perp} > R_{\parallel}$) (Fig. 2). Two test masses of mass m_1, m_2 placed within a distance $r \gg R_{\perp}$ will feel a gravitational potential dictated

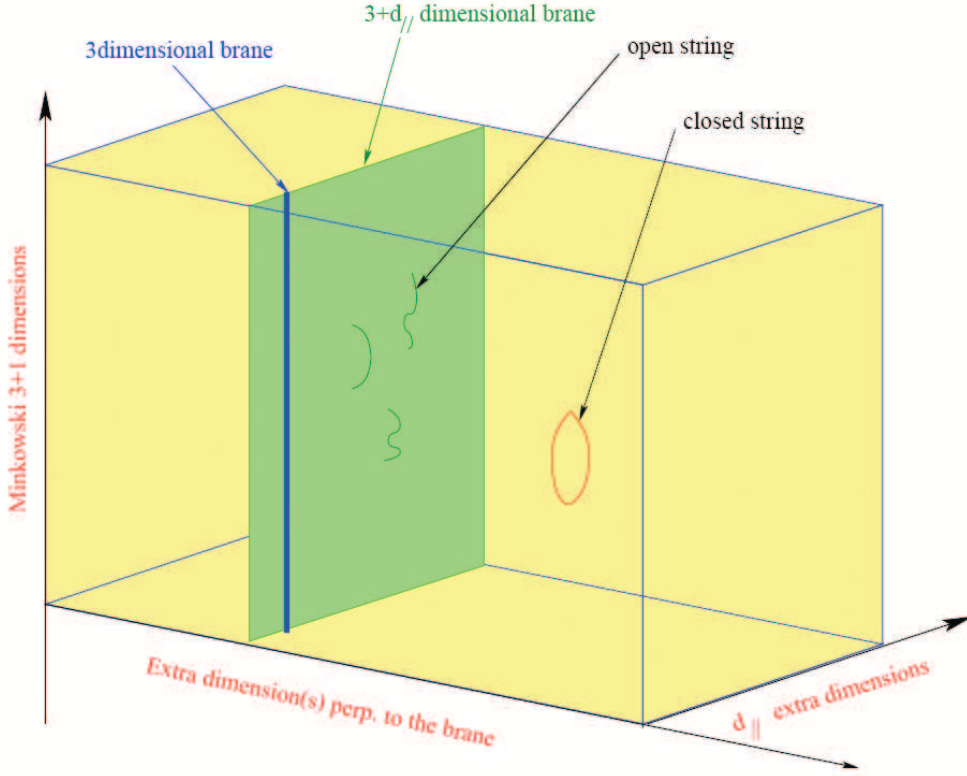


Figure 2: The string theory describes our Universe using extra dimensions. Beside the three known spatial dimensions (single blue line) there are parallel extra dimensions - p -brane (green plane) where endpoints of open strings are confined and transverse dimensions (yellow space) where only gravity can propagate (closed string) [2].

by Gauss's law in $(4 + n)$ dimensions

$$V(r) \sim \frac{m_1 m_2}{M_{Pl(4+n)}^{n+2}} \frac{1}{R_{\perp}^{n-p} R_{\parallel}^p r} \quad (1)$$

The Planck scale $M_{Pl(4+n)}$ of this dimensional theory taken to be $\sim m_{EW}$ and also $R_{\parallel}^{-1} \sim m_{EW}$.

$$V(r) \sim \frac{m_1 m_2}{m_{EW}^{n-p+2}} \frac{1}{R_{\perp}^{n-p} r} \quad (2)$$

so our effective 4 dimensional M_{Pl} is

$$M_{Pl}^2 \sim m_{EW}^{n-p+2} R_{\perp}^{n-p} \quad (3)$$

Demanding that R_\perp be chosen to reproduce the observed M_{Pl} yields ¹

$$R_\perp \sim 10^{\frac{30}{n-p}-17} \text{cm} \times \left(\frac{1 \text{TeV}}{m_{EW}} \right)^{1+\frac{2}{n-p}} \quad (4)$$

For $n - p = 1$, $R_\perp \sim 10^{13} \text{cm}$ implying deviations from Newtonian gravity over solar system distances, hence this case is empirically excluded. For all $n - p \geq 2$, however, the modification of gravity only becomes noticeable at distances smaller than those currently probed by experiments. If any SM field lived only in these p small dimensions their KK masses would be $\sim \text{TeV}$.

2.1 Kaluza-Klein Excitations

To simplify the analysis, we started with the case of $d_\parallel = 1$ compactified on S^1/Z_2 (a manifold with a discrete symmetry that identifies different points in it, here y and $-y$) where some of the gauge fields have the KK excitations in the extra dimension while fermions are localized states on brane intersections. The fermions do not have excitations and the KK momentum is not conserved while breaking of translation invariance in the extra dimension. KK models of gauge bosons are then singly produced giving rise to generally strong bounds on the compactification scale, and new resonances that can be experimentally observed by the gauge fields masses are given by (appendix A):

$$M_n^2 = M_0^2 + \frac{n^2}{R_\parallel^2} \quad (5)$$

where M_0 is the higher dimensional mass and the R_\parallel is the parallel extra dimensions. The zero mode $n = 0$ is identified with the 4d state, while the higher modes have the same quantum numbers as the lowest one, except for their mass. The ratio of the weak to strong interactions strengths leads to the conclusion that the $SU(2)$ brane

¹ $R_\perp \sim \frac{M_{Pl}^{2/(n-p)}}{m_{EW}^{1+2/(n-p)}} , M_{Pl} \sim 10^{16} \text{TeV} \Rightarrow R_\perp \sim \frac{10^{32/(n-p)}}{TeV} \times \left(\frac{TeV}{m_{EW}} \right)^{1+2/(n-p)}$

extends along the extra dimension, while $SU(3)$ does not. As a result, there are three distinct cases to study, denoted by (t, l, l) , (t, l, t) and (t, t, l) . The three positions in the brackets correspond to the three SM gauge group factors $SU(3) \times SU(2) \times U(1)$ where l stands for (longitudinal) and exists in the extra dimension, while those with t (transverse) do not [2].

Our study focused on the (t, l, l) case, where there are KK excitations of W_{\pm}^n , Z^n and γ^n . We studied the KK excitations of Z and γ which can be produced on-shell as new resonances by the neutral Drell-Yan process $pp \rightarrow l^+ l^- X$. The couplings of the excited modes to fermions is larger than the zero mode coupling by $\sqrt{2}$ for all the $n > 0$ states [8]. In order to detect and prove the existence of such KK states, we must rely on the indirect effects associated with their tower exchange.

The study is based on a number of additional assumptions, in particular, that the effect of KK exchanges is the only new physics beyond the SM. If KK excitations of SM gauge fields exist then analyses of precision electroweak data indicate that the masses of the first excitation must be greater than $\sim 4\text{TeV}$ in the case of one extra dimension [9].

2.2 Extra Heavy Boson

The deviation from the Drell-Yan SM cross section coming from KK excitations of Z and γ may be observed also in models of extra heavy boson. Grand Unified Theories (GUTs) postulate that the $SU(3)$, $SU(2)$ and $U(1)$ symmetry groups of the SM have a common origin as subgroups of some larger symmetry group G . GUT suggests that at large energy scale, this symmetry is stable. The interactions are described by local gauge theory and all the running couplings coincide. Below some critical energy scale, G is spontaneously broken and the couplings become different.

Since W , Z , γ and g are not enough to secure local gauge invariance within a large group, GUT always predicts at least one additional gauge boson arising when the symmetry is broken down to the SM.

From the various models existing we choose to look at the Z'_{SM} with SM couplings and focus on specific models coming from breaking the E_6 group which is suggested as a candidate for GUT symmetry. The models are [10]:

- $Z'_\psi : E_6 \rightarrow SO(10) \times U(1)_\psi$
- $Z'_\chi : E_6 \rightarrow SO(10) \times U(1)_\psi \rightarrow SU(5) \times U(1)_\chi \times U(1)_\psi$
- $Z'_\eta : E_6 \rightarrow SM \times U(1)_\eta$

with the following couplings:

| | g_V | g_A |
|-------|---|---|
| ν | $\frac{1}{6}\sqrt{\frac{5}{2}}\cos\theta - \frac{3}{2}\sqrt{\frac{1}{6}}\sin\theta$ | $\frac{1}{6}\sqrt{\frac{5}{2}}\cos\theta - \frac{3}{2}\sqrt{\frac{1}{6}}\sin\theta$ |
| e | $-\frac{2}{\sqrt{6}}\sin\theta$ | $\frac{1}{3}\sqrt{\frac{5}{2}}\cos\theta - \sqrt{\frac{1}{6}}\sin\theta$ |
| u | 0 | $\frac{1}{3}\sqrt{\frac{5}{2}}\cos\theta + \sqrt{\frac{1}{6}}\sin\theta$ |
| d | $\frac{2}{\sqrt{6}}\sin\theta$ | $\frac{1}{3}\sqrt{\frac{5}{2}}\cos\theta - \sqrt{\frac{1}{6}}\sin\theta$ |

Table 1: Couplings of Z' models coming from breaking the E_6 group.

where $\theta = 0, -\frac{\pi}{2}, \arctan -\sqrt{\frac{5}{3}} + \frac{\pi}{2}$ correspond to ψ, χ and η respectively.

Limits on the existence of a Z' may be divided into two categories: limits from direct searches, and limits from indirect measurements (fits to precision electro-weak data). Both direct and indirect searches lead to model-dependent constraints. The present Z' mass limits for the different models vary between 350 GeV and 1500 GeV with a good agreement between direct and indirect measurements [11]. Searches at CDF for new particles decaying to dijets [12] are indeed unable to rule out a Z' for the SSM case in any mass region.

3 The Large Hadron Collider

The LHC is a pp collider that will operate at 14TeV, center of mass energy [21]. It will be the first collider to allow the study of physics in the TeV range. The LHC was built in the former LEP tunnel at CERN, and will become operational in 2009. Table 2 compare some typical parameters of the LHC to TEVATRON experiment at Farmilab.

| | TEVATRON (Fermilab) | LHC (CERN) |
|---------------------------------------|------------------------|------------|
| Physics start date | 1987 | 2009 |
| Particles collided | $p\bar{p}$ | pp |
| Maximum beam energy (TeV) | 0.98 | 7.0 |
| Luminosity ($10^{30}cm^{-2}s^{-1}$) | 286 | 1000 |
| Time between collisions (ns) | 396 | 24.95 |
| Bunch length (cm) | $p : 50, \bar{p} : 45$ | 7.55 |
| Bunch radius ($10^{-6}m$) | $p : 28, \bar{p} : 16$ | 16.6 |
| Circumference (km) | 6.28 | 26.659 |

Table 2: High energy collider parameters for TEVATRON and LHC [13].

The main goals of the LHC include studies of the Standard Model, the discovery of the Higgs boson and searches for new physics beyond the Standard Model, such as SUSY and extra dimensions.

Before the protons are injected into the LHC, they are accelerated using a linear accelerator and the Proton Synchrotron (PS). After this, the protons are injected into the Super Proton Synchrotron (SPS) where their energies are increased up to 450 GeV. At the LHC ring, built in the former 26.7 km circumference of the LEP tunnel, the acceleration continues until the protons reach their final energy of 7 TeV. The two proton beams will collide at four interaction points along the LHC beam line with a nominal center of mass energy of 14 TeV (Fig. 3). At high

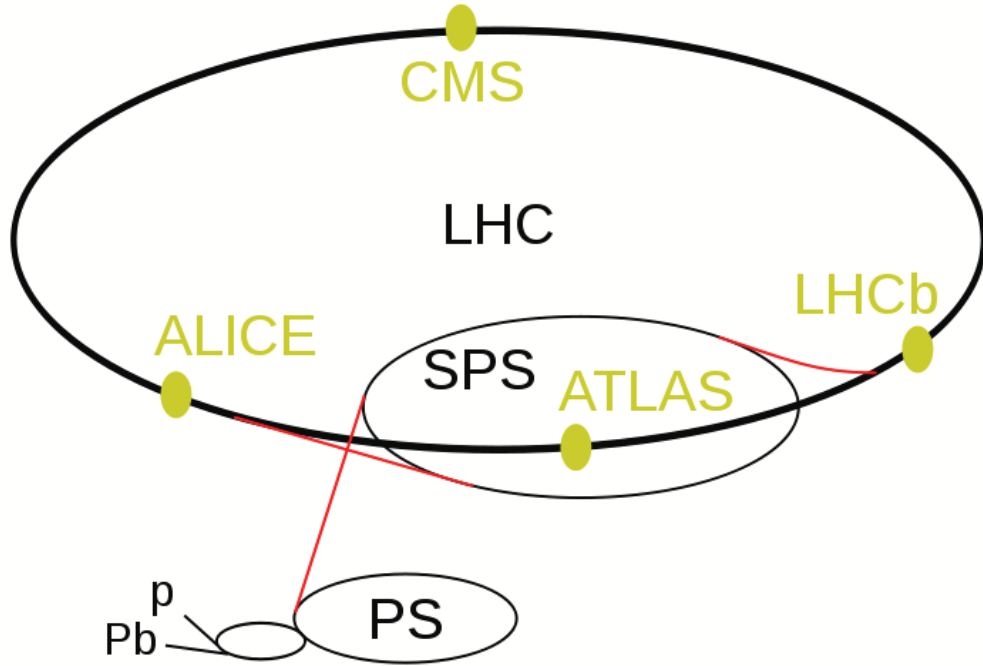


Figure 3: Overview of the accelerator complex at CERN.

luminosity the beams will be structured in 2808 bunches, 10^{11} protons each; the time interval between successive bunches is 25 ns, i.e., there will be 40,000,000 bunch-bunch collisions per second. At the beginning, the LHC collider will start with low luminosity ($10^{33} \text{cm}^{-2} \text{s}^{-1}$). After one year with low luminosity, it is planned to increase the collision rate to the highest possible luminosity of $10^{34} \text{cm}^{-2} \text{s}^{-1}$. Up to 2012 it is planned to increase the luminosity of the machine by a factor of 10 to $10^{35} \text{cm}^{-2} \text{s}^{-1}$, providing a better chance to see rare processes and improving statistically marginal measurements.

Along the LHC tunnel there are six experiments : Two multi purpose detectors, ATLAS and CMS, are designed to explore the full field of physics offered at the LHC. In addition, four dedicated experiments have been constructed. ALICE is designed to study the physics of strongly interacting matter, in particular the quark-gluon plasma, by means of Pb-Pb collisions. LHCb is a B-physics experiment that will

study CP-violation in the B-system. The aim of TOTEM is to measure the total pp cross section and to study elastic scattering. Finally, LHC will study the energy distributions of particles emitted almost parallel to the beam direction.

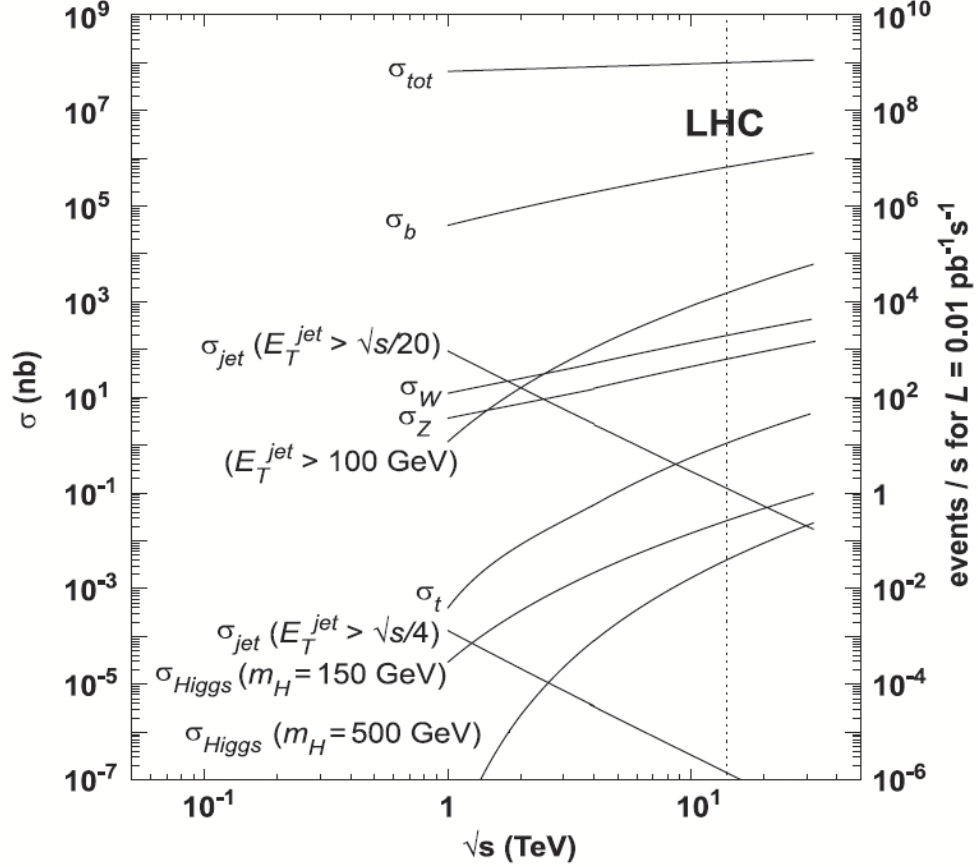


Figure 4: Proton-proton cross section of the different process as a function of the center-of-mass energy.

One of the main experimental challenges to be faced at the LHC is identifying the rare events in the vast amount of collisions. Fig. 4 shows the pp cross sections as a function of the center of mass energy for several physics processes. Indicated on the right side of the figure is the event rate assuming an instantaneous luminosity of $0.01 \text{ pb}^{-1} \text{ s}^{-1}$. The vertical line indicates the center of mass energy of the LHC. At this energy the total pp cross section is in the order of 10^8 nb , which corresponds to

an interaction rate of 10^9 events per second. Furthermore the QCD cross sections are orders of magnitude larger than the cross sections of processes such as the production of top quarks, W and Z bosons and Higgs bosons. For example the production cross section for Z bosons is one million times smaller than the total pp cross section, meaning that on average only one out of a million collisions contains a Z boson.

3.1 ATLAS Detector

One of the two multi purpose LHC detectors is the ATLAS detector [22]. It consists of a series of ever-larger concentric cylinders around the interaction point where the proton beams from the LHC collide.

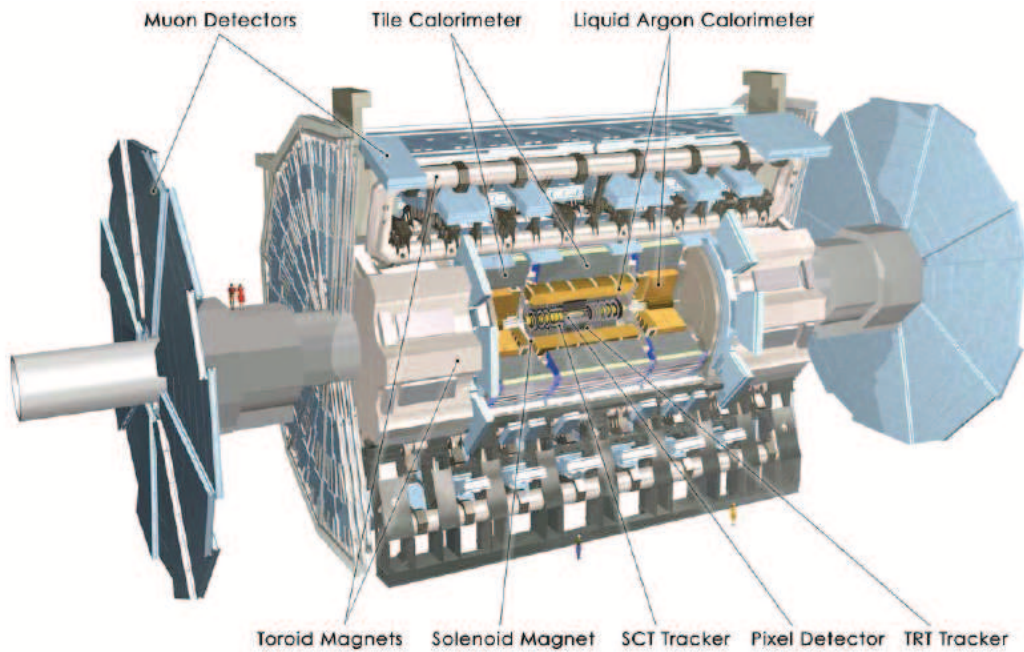


Figure 5: The ATLAS detector, with the main components highlighted.

The challenging environment in which the LHC detectors operate mean that as well as being able to accurately measure individual particles, the detectors must be fast, radiation-hard and of high granularity to be able to deal with the large particle fluxes and to be able to distinguish hits from many distinct particles in a small amount of space. In addition, requirements for the ATLAS detector were that it should have large acceptance in pseudorapidity with close to full azimuthal angle coverage, good charged particle momentum resolution and high efficiency for Inner Detector track reconstruction. Detectors as close to the beam pipe as possible were required so as to be able to have good secondary vertex resolution. In addition, excellent electromagnetic calorimetry to identify and measure electrons and photons, along with hadronic calorimetry for jet and missing transverse energy measurements, and good muon identification and momentum resolution both at low p_T and high p_T were crucial requirements. Five major parts of ATLAS are:

- **Inner Detector** - track charged particles by detecting their interaction with material at discrete points, revealing detailed information about particle momentum and charge. The inner most layers of the detector closest to the interaction point comprise the silicon pixel detector. The pixel detector is surrounded by the Semi-Conducting Tracking (SCT) detector which consists of silicon strip detectors. The outer layers of the inner detector are formed by the Transition Radiation Tracking (TRT) detector which is made of multiple layers of drift straws. The complete system is contained in a 2 Tesla solenoidal magnet.
- **Calorimeters** - measure the energy of particles by absorbing their energy. The ATLAS calorimetry consists of an electromagnetic calorimeter (ECAL), measuring the energies of electron and photons, and a hadronic calorimeter (HCAL), measuring the energies of hadrons.
- **Muon Spectrometer** - The ATLAS Muon spectrometer has been designed to provide a standalone trigger on single muons with transverse momentum of

several GeV, as well as to measure final state muons with a momentum resolution of about 3% over most of the expected momentum range. The ATLAS Muon spectrometer is a 4p detector consists of four types of detector technologies. Monitored Drift Tube (MDT) chambers and Cathode Strip Chambers (CSC) are used for the precision measurement of muon tracks. Resistive Plate Chambers (RPC) are employed for triggering muons in the barrel region where Thin Gap Chambers (TGC) stations serve the same purpose in the higher background region of the end-cap. The TGCs were designed and constructed at a collaboration of China, Japan and Israel (Weizmann institute, Technion and Tel Aviv University) and were tested at the Tel Aviv cosmic hodoscope before their installation at the ATLAS detector.

- **Magnet Systems** - bend charged particles in the Inner Detector and the muon spectrometer, allowing their momenta to be measured. The magnet system of the muon spectrometer consists of three air-core toroids. Each toroid is build up of eight super conducting coils assembled in a radial configuration. Due to the finite number of coils, the field is not perfectly toroidal. The deviations are most profound in the transition region between the barrel and the end-caps. The magnets provide an average bending power of 3 Tm in the barrel and 6 Tm in the end-caps.
- **Forward detectors** - measure elastic scattering at very small angles in order to get a handle on the absolute luminosity at the interaction point of ATLAS.

The detection of our signal requires momentum and charge measurement of the $\mu^-\mu^+$ and e^-e^+ coming from Z^* or Z' decay. In $\mu^-\mu^+$ we measure the curvature of their trajectory in magnetic field, both in the Inner Detector and the Muon Spectrometer. The performance goal for the muon spectrometer is the achievement of a standalone p_T resolution of 10% on a 1 TeV muon. The contributions of various factors to momentum resolution, as a function of transverse momentum, are shown in Fig. 6. The resolution is worse in the higher p_T region.

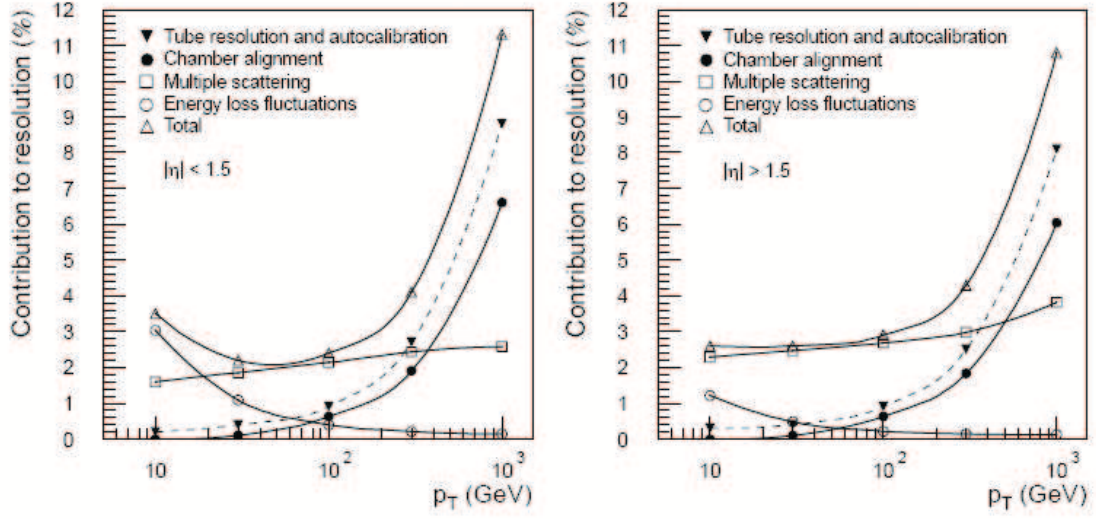


Figure 6: Momentum resolution for muons reconstructed in the Muon Spectrometer as a function of transverse momentum averaged over $|\eta| < 1.5$ (left plot) and averaged over $|\eta| > 1.5$ (right plot).

With the e^-e^+ pairs it is the opposite case. Their momentum is measured at the Inner detector while their energy is measured by the EM Colorimeter which dominate at high energy ($E > 200\text{GeV}$), with an expected resolution given by

$$\frac{\Delta E}{E} = \frac{11.5\%}{\sqrt{E(\text{GeV})}} \oplus 0.5\% \quad (6)$$

were the measurement accuracy improves with growing energy.

4 Expected Sensitivity at the LHC

To calculate the sensitivity for New Physics discovery (or exclusion) at the LHC, an integrated luminosity of 10 fb^{-1} is assumed. This is the integrated luminosity expected to be achieved during 2009. Electrons and muons are expected to be observed at the LHC detectors at the pseudo-rapidity range $|\eta_l| < 2.5$, and in order to avoid fake leptons, a requirement on the lepton transverse momentum, p_T^l , to exceed $10 \text{ GeV}/c$ is envisaged. Both η_l and p_T^l are measured in the laboratory frame with respect to the beam direction. It is assumed that within these two kinematic bounds, the efficiency will be close to 100%. Another possible cut would be an upper bound on the p_T of the di-lepton system and/or of the jets accompanying the leptons. This cut would reject almost all tau-pair events, lepton-pair events originating from di-bosons and other processes where the Drell-Yan pairs are accompanied by other high p_T particles, e.g. radiative QCD and QED events. The effect of this last cut on the Leading Order (LO) Drell-Yan electron and muon pairs is assumed to be negligible.

The event sample obtained after all cuts mentioned above is assumed to be composed almost entirely of di-electron and di-muon Drell-Yan pairs, produced via a s-channel photon, Z and possibly also Z' or Kaluza-Klein excitations of the photon and the Z. Any other contribution is neglected.

Signals for New Physics can be seen both in the distribution of the di-lepton invariant mass, $M = \sqrt{\hat{s}}$, and in the forward-backward asymmetry. The cuts on the lepton p_T and pseudo-rapidity can affect these two observables. The cut efficiency as a function of M , $\epsilon(M)$ is not affected by the presence of a New Physics signal. For a given value of M , the New Physics signal modifies only the forward-backward asymmetry, but for an symmetric detector, this would not affect the efficiency.

Two methods have been used to estimate $\epsilon(M)$. The first one is based on

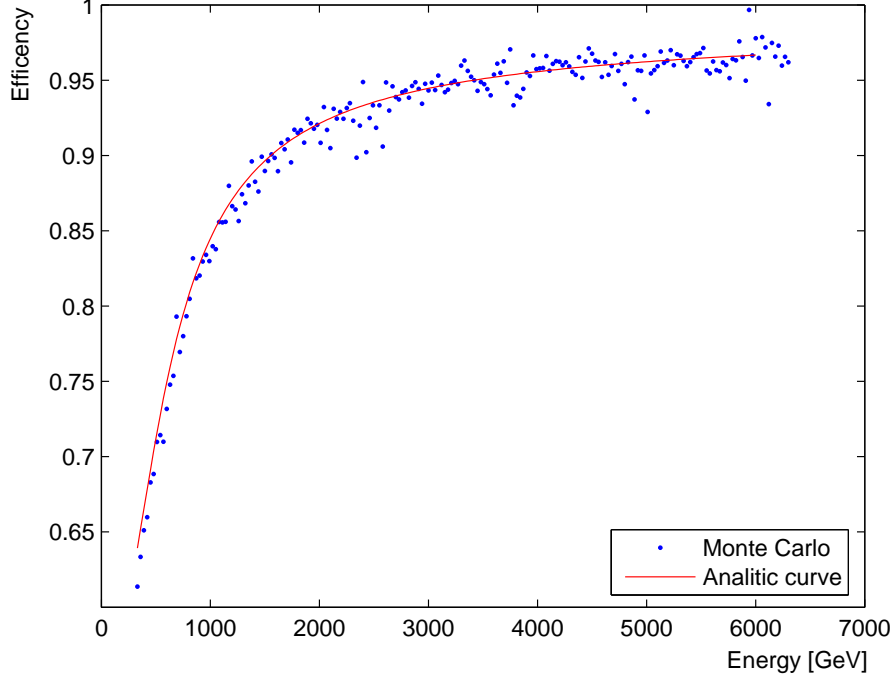


Figure 7: Efficiency as a function of invariant mass. For each energy we calculate the numbers of expected events with and without the cuts on rapidity and p_T . The plot represents the ratio of the di-lepton mass distributions with and without those cuts

Monte Carlo method, and the other on analytic calculations. In the first method, the PYTHIA6.2 [15] Monte Carlo program has been used to generate Standard Model di-lepton events. The cuts on p_T and pseudo-rapidity have been applied, and $\epsilon(M)$, shown in Fig. 7 by the solid points, is simply the ratio of the di-lepton mass distributions with and without theses cuts.

For the second method to estimate $\epsilon(M)$, the differential cross section with respect to M and $\cos \theta^*$ is needed, where θ^* is the angle between the outgoing ℓ^- and the incoming quark. This cross section is given by,

$$\frac{d^2\sigma(pp \rightarrow \ell^- \ell^+ X)}{dM d\cos \theta^*} = \frac{4}{3M} \sum_{q=d,u,s,c} \frac{d\sigma(q\bar{q} \rightarrow \ell^- \ell^+)}{d\cos \theta^*} \cdot \int dy x_1 f_q(x_1, M^2) x_2 f_{\bar{q}}(x_2, M^2) \quad (7)$$

where y is the rapidity of the di-lepton system, f_q and $f_{\bar{q}}$ are the Parton Distribution

Functions (PDF's) of the quark and anti-quark, and the Bjorken x variables are given by, $x_{1,2} = \frac{M}{2E_{\text{beam}}} \cdot e^{\pm y}$. The factor $4/(3M)$ accounts for the Jacobian of the transformation from $dx_1 dx_2$ to $dy dM$ ($2/M$), the factor 2, allows both quarks and antiquarks to originate from both protons, and a color factor ($1/3$) is due to the final state being a color singlet, whereas the PDF's correspond to the quark or antiquark distributions at any color.

The differential $q\bar{q} \rightarrow \ell^- \ell^+$ cross section is given by,

$$\frac{d\sigma(q\bar{q} \rightarrow \ell^- \ell^+)}{d\cos\theta^*} = \frac{\pi\alpha^2}{8M^2} \sum_{\lambda, \lambda'=\pm 1} \left| (\mathcal{A}^\gamma + \mathcal{A}_{\lambda, \lambda'}^Z + \mathcal{A}_{\lambda, \lambda'}^{\text{NP}})(1 + \lambda\lambda' \cos\theta^*) \right|^2, \quad (8)$$

where λ and λ' are the helicity signs of the incoming quark and the outgoing negative lepton respectively. The photon and Z s-channel amplitudes, are given by,

$$\mathcal{A}^\gamma = Q_q Q_\ell, \quad \mathcal{A}_{\lambda, \lambda'}^Z = \frac{g_q^\lambda g_\ell^{\lambda'} M^2}{M^2 - M_z^2 + iM^2 \Gamma_z / M_z}, \quad (9)$$

with,

$$g_f^+ = \frac{-Q_f \sin^2 \theta_w}{\sin \theta_w \cos \theta_w} \quad g_f^- = \frac{I_f^3 - Q_f \sin^2 \theta_w}{\sin \theta_w \cos \theta_w} \quad f = q, \ell \quad (10)$$

where Q_f is the fermions charge in units of the positron charge and θ_w is the weak mixing angle. In the case of Z', the New Physics amplitude is given by the same expression as for the Z (eq. 9), but with different values for the mass, total width and couplings. Similarly, for Kaluza Klein excitations,

$$\mathcal{A}_{\lambda, \lambda'}^{\text{NP}} = \sum_{n=1}^{\infty} \left(\mathcal{A}^{\gamma_n} + \mathcal{A}_{\lambda, \lambda'}^{Z_n} \right), \quad (11)$$

where,

$$\mathcal{A}^{\gamma_n} = \frac{2Q_q Q_\ell M^2}{M^2 - M_{\gamma_n}^2 + iM^2 \Gamma_{\gamma_n} / M_{\gamma_n}} \quad \mathcal{A}_{\lambda, \lambda'}^{Z_n} = \frac{2g_q^\lambda g_\ell^{\lambda'} M^2}{M^2 - M_{z_n}^2 + iM^2 \Gamma_{z_n} / M_{z_n}}, \quad (12)$$

with the factor 2 in the numerators accounting for the couplings of the Kaluza Klein excitations being enhanced by $\sqrt{2}$ compared to the Standard Model ones [8].

For the efficiency calculation, the New Physics amplitude can be omitted, since, as explained above, it is not expected to have any effect. The integration of the

differential cross section with respect to $\cos\theta^*$ has to be performed with and without the cuts. Without the cuts, $\cos\theta^*$ can vary in its full range, between -1 and 1, yielding the *produced* differential cross-section with respect to M , namely, the produced M distribution. The effect of the selection cuts is to limit the allowed range of $\cos\theta^*$. The lepton transverse momentum, p_T^l , is invariant under the boost of the dilepton system and can be calculated in the lepton rest-frame. Neglecting the lepton mass, the requirement $p_T^l > 10$ GeV corresponds to $|\cos\theta^*| < \sqrt{1 - (20\text{GeV}/M)^2}$, resulting in a requirement on M to exceed 20 GeV. The requirement $|\eta| < 2.5$ corresponds to, $|\cos\theta^*| < \tanh(2.5 - |y|)$ and consequently, $|y|$ is constrained to be below 2.5. The resulting integral over y and $\cos\theta^*$ within these cuts yields the *visible* M distribution. The efficiency, which is the ratio between the visible and the produced distributions, is plotted in Fig. 7 by the solid line, which agrees with the results of the Monte Carlo calculation.

Two different strategies are used in order to search for a New Physics signal and, in case such signal is observed, to distinguish between Z' and Kaluza Klein excitations of the photon and the Z .

- Search for peaks in the di-lepton invariant mass distribution.
- Measure the forward-backward charge asymmetry.

These strategies will be detailed in the following sub-sections.

4.1 Di-Lepton Invariant Mass

To study the Di-lepton mass distribution, we simulated the generation of di leptons in the pp collision using the PYTHIA6.2 Monte Carlo program has been used. The

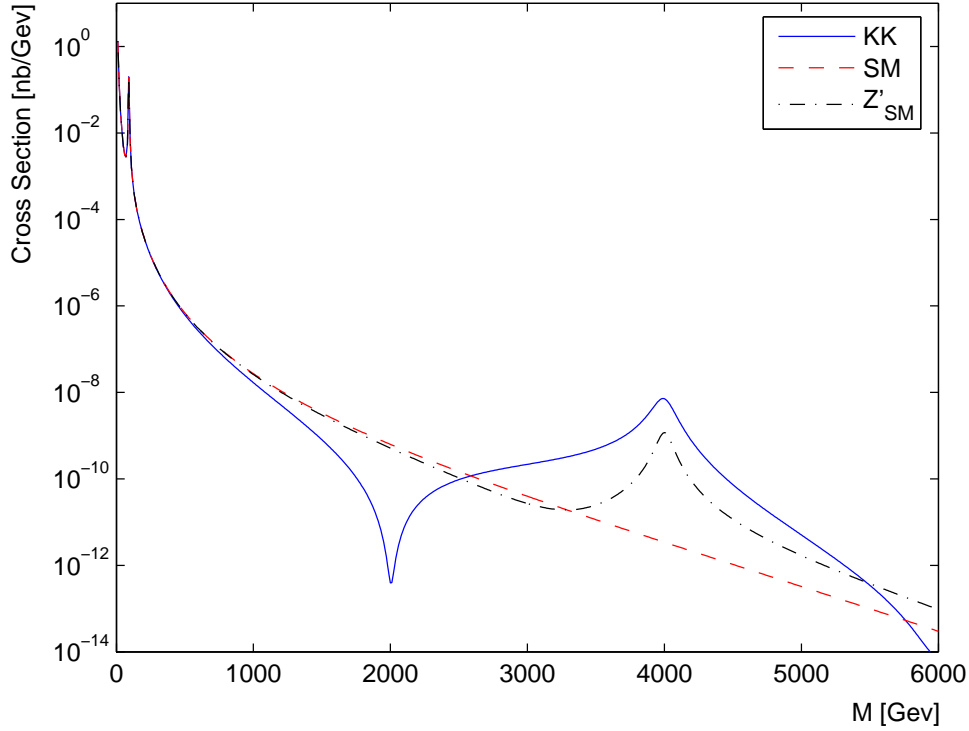


Figure 8: Di-lepton mass distribution before the cuts. Dashed curve shows the expected SM distribution with peak of the Z^0 is seen at 90 GeV. The solid curve shows the KK excitations with the first excited state mass set to 4TeV, and the dash dot curve - the Z' .

events were generated with a center-of-mass energy above 10 GeV, and their total number corresponds to an integrated luminosity of 10 fb^{-1} . The leptons have been required to pass the kinematic cuts on p_T^l and η_l listed above. Fig. 8 shows the distribution of the di-lepton mass, M . The dashed curve shows the expected Standard Model visible distribution which is considered in this analysis as background. This curve has been calculated by multiplying the integrated luminosity with the visible differential cross section calculated in the previous sub-section without the contribution of the New Physics amplitude. The CTEQ6 PDF's [16], as implemented in the LHAPDF library [17], have been used.

The cross section used corresponds to Leading Order (LO) in QCD. The effect

of the Next to Leading Order (NLO) can be approximated as an increase by a K-factor of ≈ 1.26 [18], almost independent of the di-lepton energy. This K-factor is assumed to be the same also for the signal, based on calculations done for the Z [19] and for some particular Z' model [20]. However, a large part of this correction to the LO cross section is due to events of di-leptons accompanied with jets. As already mentioned above, most of these events can be rejected by the selection procedure, reducing the overall NLO correction on the cross section multiplied by the selection efficiency to a value lower than the quoted K-factor of 1.26. This value, depending on the selection cuts, is a priori unknown, resulting an uncertainty on the overall normalization. Other contributions to this normalization error come from the uncertainties on the integrated luminosity and on the overall selection efficiency.

Since the generator is based on the SM knowledge, the agreement between the generated pseudo-data distribution and the Standard Model curve is perfect, leaving very small room for a possible New Physics signal contribution. In order to quantify our sensitivity for New Physics, a contribution of a possible signal, $\frac{ds(E)}{dE}$, is considered. This is done in a model-independent way, having a Breit-Wigner resonance shape with a width arbitrarily assumed to be $0.1M$, where M is the resonance mass. Here we neglect the effects of the PDF's and the detector resolution on the resonance shape, based on the assumption that the detailed shape of the resonance does not affect our sensitivity, as long as the area under the resonance stays the same. The interference between the resonance contribution and the Standard Model background is neglected as well. This assumption is part of our model-independent approach, since any interference term would depend on the particular values of the couplings of the resonance which are model dependent. The justification for this approximation is related to the fact that our sensitivity to the resonance is dominated by events close to its maximum, where its amplitude is mostly imaginary, whereas the amplitude of the Standard Model background, being far above the photon and the Z masses, is real.

The resonance function is then given by,

$$\frac{ds(E)}{dE} = \sigma_s \cdot \frac{dw(E)}{dE} \cdot \int \mathcal{L} dt \quad (13)$$

where σ_s is the total visible signal cross section corresponding to LO QCD, $\frac{dw(E)}{dE}$ is the Breit-Wigner resonance shape function, normalized to unity and $\int \mathcal{L} dt$ is the integrated luminosity. As already explained above, the efficiency of the signal detection is expected to be the same as for the background, depending only on M .

A binned maximum likelihood method with Poisson statistics is used to set an upper limit on σ_s . The likelihood function is defined as,

$$L(\sigma_s) = \prod_{i=1}^N \frac{(b_i + s_i)^{n_i} e^{-(b_i + s_i)}}{n_i!} \quad (14)$$

where the product is over all the bins in the energy distribution, n_i is the number of pseudo-data events in bin i , b_i , is the expected number of background events on that bin corresponding to energy E_i , and similarly s_i for signal events. The dependence on σ_s enters through s_i . However, to account for the overall normalization uncertainty, the Likelihood function is modified to,

$$L'(\sigma_s, x) = \prod_{i=1}^N \frac{[(b_i + s_i)(1 + x)]^{n_i} e^{-(b_i + s_i)(1+x)}}{n_i!} \quad (15)$$

where x is the relative change in the expected number of signal and background events. For each value of σ_s , $L'(\sigma_s, x)$ has to be maximized with respect to x , yielding $L'_{max}(\sigma_s)$. In this way, the overall normalization is determined from the data, mainly at the low energy region where the event statistics is high. Thus, the uncertainties from the NLO effect, efficiency and luminosity errors do not affect the analysis, as long as they are energy independent.

To calculate the upper limits for σ_s , the Bayesian approach is adopted, interpreting the likelihood to be proportional to the probability distribution function of σ_s . The 95% c.l. (exclusion) limit in σ_s , σ_s^{95} , is then calculated as,

$$\int_{\sigma_s^{95}}^{\infty} L'_{max}(\sigma_s) d\sigma_s = 0.05 \cdot \int_0^{\infty} L'_{max}(\sigma_s) d\sigma_s \quad (16)$$

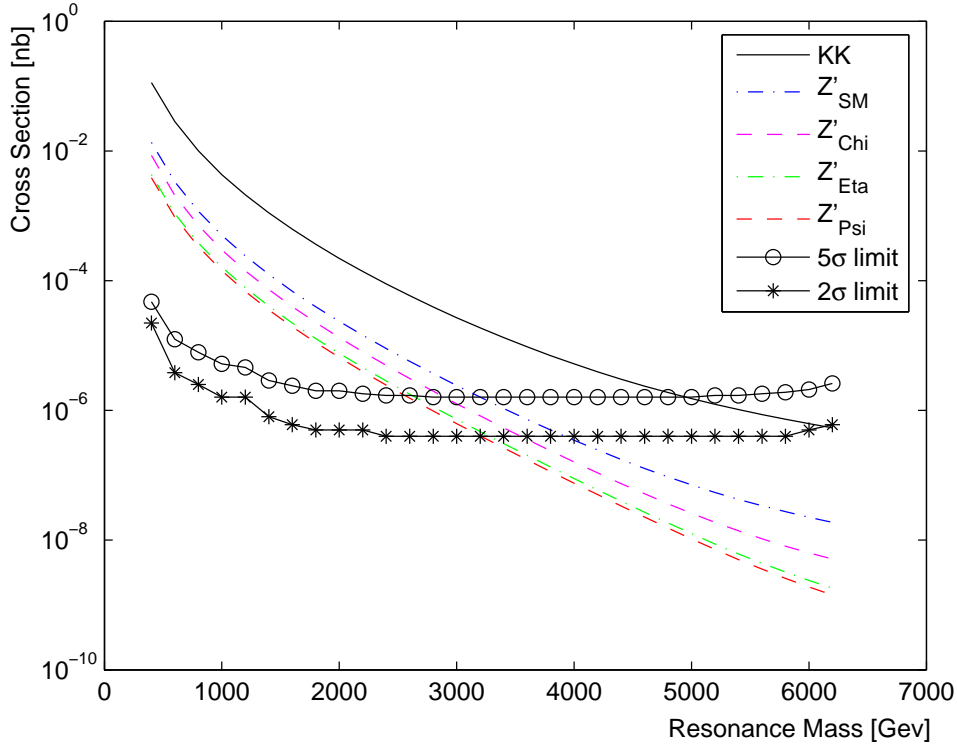


Figure 9: Expected visible cross sections for the various Z' models and for the KK model compared with the cross section upper limit of 2σ and 5σ . The crossing points corresponds to the upper limits of the resonance mass which can be excluded/discovered at the LHC corresponding to integrated luminosity of 10fb^{-1} .

A similar expression holds for the 5σ (discovery) limit, where the factor 0.05 is replaced with $5.7 \cdot 10^{-7}$. These limits are plotted in Fig. 9.

In order to test our assumption that the resonance shape and width have a very small effect on the limits, the calculation has been repeated with a Gaussian shape, replacing the Breit-Wigner resonance shape. This modification corresponds to moving from the case where the resonance width is dominated by its natural width, to the case where it is dominated by the detector resolution. Another modification was to increase the resonance width from a narrow ($0.1M$) to a much larger ($0.7M$). The resonance width is expected to cover the natural width and the detector resolution

| | Z_{KK}^* | Z'_{SM} | Z'_χ | Z'_η | Z'_ψ |
|---------------------------------|------------|-----------|-----------|-----------|-----------|
| Mass Limits for 2σ [GeV] | 6135 | 3922 | 3544 | 3277 | 3206 |
| Mass Limits for 5σ [GeV] | 4953 | 3200 | 2893 | 2623 | 2557 |

Table 3: Mass limits for integrated luminosity of 10fb^{-1}

which depends on lepton energy and, as explained in the previous section, for high lepton energy corresponding to high resonance mass, is expected to be much better for electrons than for muons. Both width and shape modifications resulted in very small changes, 1% – 5%, justifying our model-independent approach.

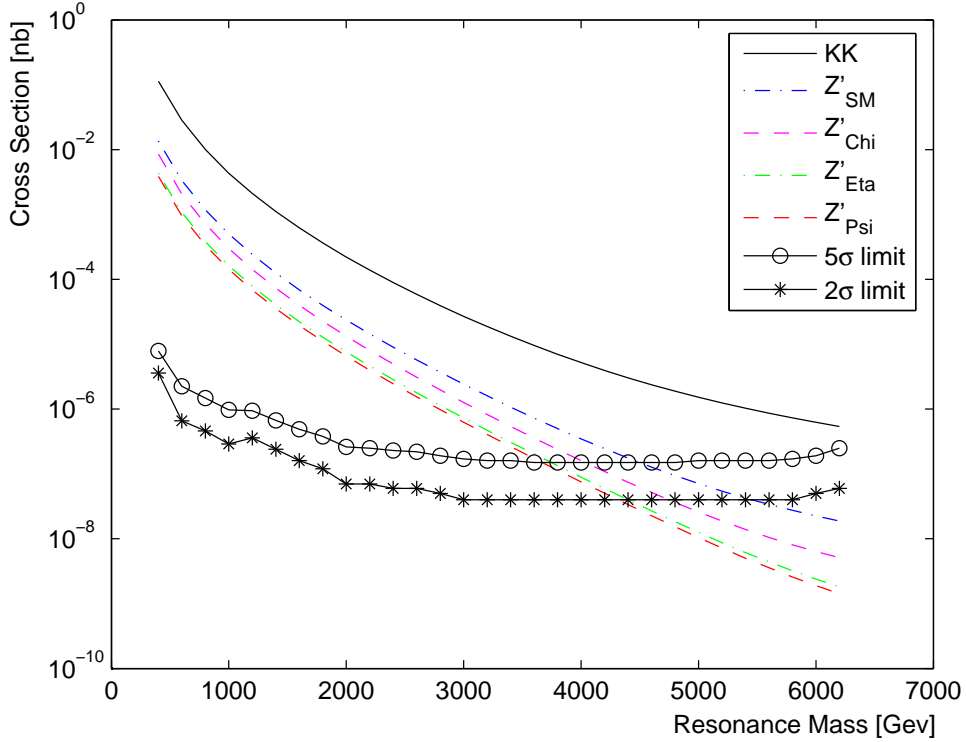


Figure 10: Expected visible cross sections for the various Z' models and for the KK model compared with the cross section upper limit of 2σ and 5σ . The crossing points corresponds to the upper limits of the resonance mass which can be excluded/discovered at the LHC corresponding to integrated luminosity of 100fb^{-1} .

The calculated upper limits should be compared to the expected visible cross

sections for the various Z' models and for the Kaluza Klein model described above. Since the upper limits correspond to LO QCD, it is sufficient to calculate the expected visible cross sections in LO QCD using the expressions in the previous subsection and taking into account the selection cuts on η_l and p_T^l as explained above. The contributions of the Standard Model amplitudes have been subtracted, leaving only the contributions of the New Physics terms and their interference with the Standard Model amplitudes. The cross-section is plotted in Fig. 9 as function of the resonance mass, M , for the various models. The crossing points of these lines with the 95% (5σ) upper limit lines correspond to the upper limits of resonance mass which can be excluded (discovered) at the LHC. These mass limits are listed in Table 3.

We repeated the study with total numbers of events corresponding to an integrated luminosity of 100 fb^{-1} , see Fig. 10 and Table 4.

| | Z_{KK}^* | Z'_{SM} | Z'_χ | Z'_η | Z'_ψ |
|---------------------------------|------------|-----------|-----------|-----------|-----------|
| Mass Limits for 2σ [GeV] | 7521 | 5451 | 4745 | 4397 | 4313 |
| Mass Limits for 5σ [GeV] | 6564 | 4496 | 4034 | 3746 | 3668 |

Table 4: Mass limits for integrated luminosity of 100 fb^{-1}

Our limits are much higher than the CDF II limits obtained at $\sqrt{s} = 1.96 \text{ TeV}$ $p\bar{p}$ collision with integrated luminosity of 1.3 fb^{-1} . In CDF, the Z_{SM} is found to be excluded for masses below 923 GeV and the E_6 Z' bosons: the Z'_ψ , the Z' and the Z'_η are excluded with masses below 822, 822 and 891 GeV respectively [14].

4.2 Forward-Backward Asymmetry

The forward-backward asymmetry is defined as,

$$A_{\text{FB}} = \frac{\sigma(\cos \theta^* > 0) - \sigma(\cos \theta^* < 0)}{\sigma_{\text{tot}}}. \quad (17)$$

Unfortunately, the angle θ^* , which is the angle of the outgoing negative lepton with respect to the incoming quark direction, cannot be directly measured at a proton-proton collider like LHC, since the incoming quark direction cannot be distinguished from the direction of the antiquark. However, in many cases, the incoming quark is a valence quark, and is more energetic than the anti-quark coming always from the sea. In these cases, the direction of the incoming quark coincides with the direction of the overall momentum, or the boost of the quark-antiquark system which is the same as the di-lepton system and can be measured. Therefore, the measurable quantity, is the asymmetry with respect to the boost,

$$A_{\text{FB}}^{\text{boost}} = \frac{1}{\sigma_{\text{tot}}} \times (\sigma(\cos \theta^* > 0, y > 0) + \sigma(\cos \theta^* < 0, y < 0) - \sigma(\cos \theta^* > 0, y < 0) - \sigma(\cos \theta^* < 0, y > 0)) \quad (18)$$

and this is the asymmetry we refer to in the following.

To get a more detailed formula for the asymmetry, we start from the SM differential cross section. Similar to Eq.(7), we can write it by:

$$\frac{d^2\sigma}{dM d\cos \theta^*} \sim \sum_{i=1}^8 (A_i(1 + \cos^2 \theta^*) + 2B_i \cos^2 \theta^*) \int dy f_i(x_1, M^2) f_i(x_2, M^2) \quad (19)$$

where $i = u, d, c, s, \bar{u}, \bar{d}, \bar{c}, \bar{s}$ and:

$$A_i \equiv \frac{s}{4} \sum_{\lambda, \lambda'} \left| \frac{g_q^\lambda g_l^{\lambda'}}{s - M_z^2 + i M_z \Gamma_z} + \frac{Q_q Q_l}{s} \right|^2$$

$$B_i \equiv \frac{s}{4} \left[\sum_{\lambda=\lambda'} \left| \frac{g_q^\lambda g_l^{\lambda'}}{s - M_z^2 + i M_z \Gamma_z} + \frac{Q_q Q_l}{s} \right|^2 - \sum_{\lambda \neq \lambda'} \left| \frac{g_q^\lambda g_l^{\lambda'}}{s - M_z^2 + i M_z \Gamma_z} + \frac{Q_q Q_l}{s} \right|^2 \right] \quad (20)$$

Now, the forward and backward events are given by:

$$\begin{aligned}
A_f &= \sigma(\cos\theta^* > 0) = \int_0^k d(\cos\theta) \frac{d\sigma}{dM} = \int \sum_i \left(A_i k + \frac{A_i}{3} k^2 + B_i k^2 \right) \times \\
&\quad f_i(x_1, M^2) f_i(x_2, M^2) dy \\
A_b &= \sigma(\cos\theta^* < 0) = \int_{-k}^0 d(\cos\theta) \frac{d\sigma}{dM} = \int \sum_i \left(A_i k + \frac{A_i}{3} k^2 - B_i k^2 \right) \times \\
&\quad f_i(x_1, M^2) f_i(x_2, M^2) dy \quad (21)
\end{aligned}$$

where k coming from the cuts (rapidity and P_T) and the sum on i represents summing on the quarks and anti-quarks ($i = 1, 2, \dots, 8$). As we already saw, the measurable quantity, is the asymmetry with respect to the boost. Hence, when we summarize the quarks and anti-quarks, we add the backward events of the anti-quarks to the forward events of the quarks and vice versa,

$$\begin{aligned}
A_f^{Boost} &= \int_0^{R_{max}} (A_f(q) + A_b(\bar{q})) f_q(x_1, M^2) f_{\bar{q}}(x_2, M^2) dy + \\
&\quad \int_{R_{min}}^0 (A_b(q) + A_f(\bar{q})) f_q(x_1, M^2) f_{\bar{q}}(x_2, M^2) dy \\
A_b^{Boost} &= \int_0^{R_{max}} (A_b(q) + A_f(\bar{q})) f_q(x_1, M^2) f_{\bar{q}}(x_2, M^2) dy + \\
&\quad \int_{R_{min}}^0 (A_f(q) + A_b(\bar{q})) f_q(x_1, M^2) f_{\bar{q}}(x_2, M^2) dy \quad (22)
\end{aligned}$$

where $R_{max} = -0.5 \ln\left(\frac{s}{s_{max}}\right)$ and $R_{min} = 0.5 \ln\left(\frac{s}{s_{max}}\right)$ are the maximum and the minimum rapidity. Finally, we get the forward-backward asymmetry,

$$A_{FB} = \frac{A_f^{boost} - A_b^{Boost}}{A_f^{boost} + A_b^{Boost}} \quad (23)$$

Due to the selection cuts, events with large $|\cos\theta^*|$, where the asymmetry is maximal, are rejected. Consequently, the magnitude of the observed asymmetry is expected to be reduced, compared with the produced sample before cuts. Fig. 11 shows the expected asymmetry as a function of M for Z' at 4TeV with Standard Model couplings and for Kaluza Klein excitations with a mass scale of 4TeV. The SM asymmetry is very similar to the asymmetry of the KK just without the peak in region *I* and the deep in region *II*. The dashed-dotted (solid) line describes

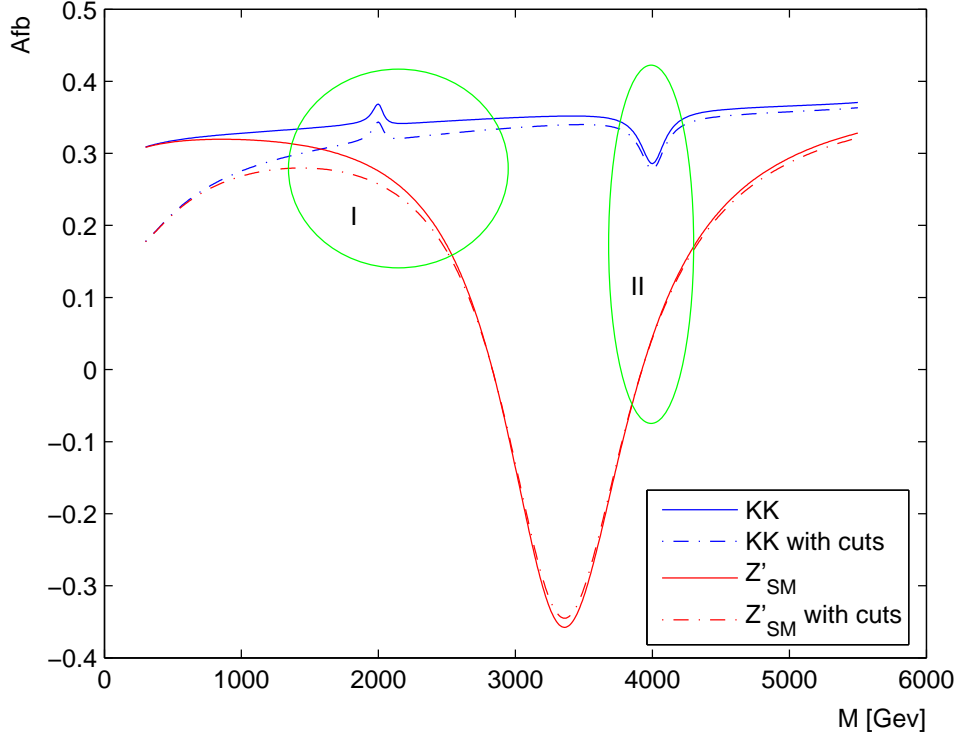


Figure 11: Forward-Backward Asymmetry for the KK excitations and the Z'_{SM} , with and without the cuts: $P_T > 10$ GeV, $|y| < 2.5$. The asymmetry was calculated with respect to the boost direction.

the asymmetry without (with) the selection cuts. As demonstrated in Fig. 7 the efficiency increases with the mass and therefore the cuts impact on the asymmetry is diminishing.

The asymmetry for the case of Kaluza Klein excitations is rather close to the Standard Model one, since the Standard Model Z^0 , as well as its excited state Z^* , is always accompanied by γ or γ^* . Far from any resonance, the main contribution to the asymmetry is from the γ/Z interference, and this is the same for both models. Only near the resonances there are differences which are rather small. On the other hand, a Z' is not accompanied by a γ , and therefore, its asymmetry, even at M region quite far below the resonance mass differs significantly from the SM case.

Due to the LHC finite statistics, it will not be possible to precisely measure the full dependence of the asymmetry on M . If a resonance is seen at the M distribution, it would be possible to measure the asymmetry at the resonance region, in order to try and distinguish between the different models. Alternatively, even if no resonance is observed, we can attempt to evaluate the asymmetry deviation from the SM predicted value.

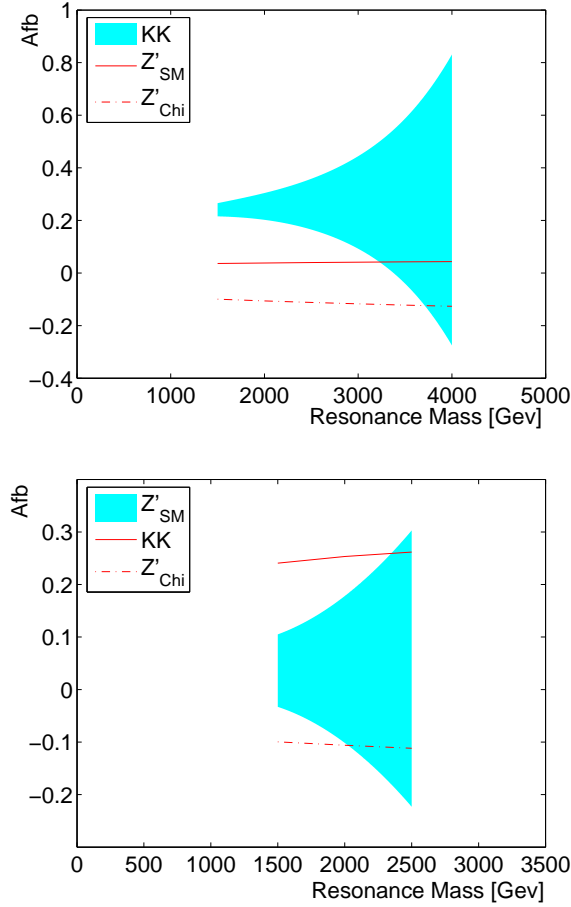


Figure 12: Upper plot: forward-backward asymmetry of the KK resonance with 3σ errors (painted area), asymmetry of the Z'_{SM} resonance without the errors (solid line) and asymmetry of the Z'_{χ} resonance without the errors (dashed-dotted line). Bottom plot: forward-backward asymmetry of the Z'_{SM} resonance with 3σ errors (painted area), asymmetry of the KK resonance without the errors (solid line) and asymmetry of the Z'_{χ} resonance without the errors (dashed-dotted line).

In a case when the resonance is observable at the M distribution, we can focus our study on the region II in Fig. 11. In spite of the large difference between the Z' and the SM asymmetry's, it does not provide us enough information for discovery and even not for exclusion, as can see at Fig. 14. We demonstrate the significance of separating the Z' from SM, by defining the significance as,

$$Sig^{Z'/SM} = \left| \frac{A_{\text{FB}}^{Z'} - A_{\text{FB}}^{SM}}{\Delta A_{\text{FB}}^{Z'}} \right| \quad (24)$$

The forward-backward asymmetry error, ΔA_{FB} , is calculated in the following way. We can write the asymmetry as:

$$A_{\text{FB}} = \frac{N_f - N_b}{N_f + N_b} = 2P - 1 \quad (25)$$

where $p = \frac{N_f}{N}$ and $N = N_f + N_b$. The asymmetry error is given from the binomial error on P :

$$\Delta A_{\text{FB}}^{Z'} = 2\Delta P = 2\sqrt{\frac{P(1-P)}{N}} \quad (26)$$

The forward-backward asymmetry can be also used to distinguish between the Z' and KK cases. Fig. 12 depict the asymmetries as a function of the resonance mass, corresponding to an integrated luminosity of 10fb^{-1} . One can clearly see the distinction between the KK model and Z'_{SM} model in both cases: when we take the KK model with errors (3σ) and the Z'_{SM} without errors and vice versa. Since the KK cross section is larger than Z'_{SM} , we get more events if $Z_K K$ exists and the errors are smaller compared to the Z'_{SM} errors. Therefore, we can get a better separation between KK and Z' models when we take into account the KK errors. Obviously, this question as to which error to take will not be present when we get real data, and the errors will be determined then by the number of real data events. In the upper plot we show that we can distinguish between KK model from Z'_{SM} model up to a mass of 3250GeV and KK model from Z'_χ model up to a mass of 3750GeV . All other Z' models are located between Z'_{SM} and Z'_χ .

In order to compare between the two methods to distinguish between the KK and Z' models (cross section comparison and forward-backward asymmetry), in the

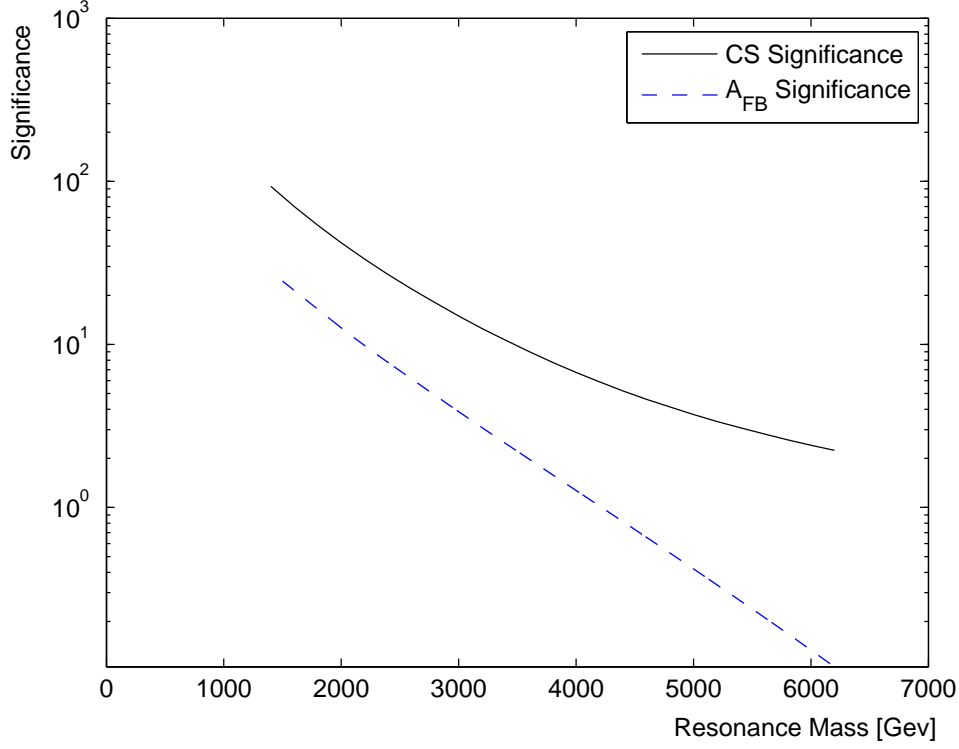


Figure 13: The significance for distinction between the Z'_{SM} and the KK model by cross section and forward-backward asymmetry measurements on the peak, corresponding to $\int Ldt = 10\text{fb}^{-1}$

case with observable resonance in the M distribution, we defined the significance in the following way: For the forward-backward asymmetry:

$$Sig^{A_{FB}} = \frac{A_{FB}^{KK} - A_{FB}^{Z'}}{\Delta A_{FB}^{KK}} \quad (27)$$

where ΔA_{FB}^{KK} is defined as before. For the cross section we use:

$$Sig^{CS} = \frac{KK_{Events} - Z'_{Events}}{\sqrt{KK_{Events}}} \quad (28)$$

where $KK_{Events} = \sigma_{KK} \int Ldt$ and σ_{KK} is the integrated cross section. In Fig. 13 we show both significances as a function of the resonance mass. As seen in the figure the contribution of the cross section measurement is much more significant than the

asymmetry contribution and we can distinguish between the models by looking at the cross section alone.

4.3 Invisible Resonance

If we don't observe the resonance in the M distribution, which may happen if the luminosity is low or the mass of the resonance is too high to be detected at the LHC, we would like to focus on the lower energies and search for deviations from the SM that are caused by the unseen Z^* or Z' resonance existence. Fig. 8 and Fig. 11 suggest that in the case of Z^* the deviation from the SM is more pronounced in the cross section distribution while in the Z' case the distinction is much more significant in the asymmetry distributions. In both cases we would like to integrate over energies lower than the resonance energy for each model separately.

In order to do that, we define a semi-arbitrary point for each model ($P_{CS}, P_{A_{FB}}$), where the distributions start to differ from the SM distribution. We found that the dependence of those points on the resonance mass is approximately linear. Using that relation for a given mass we can choose the lower integration bounds. The high boundary makes sure the resonance will not contribute to the calculations.

In order to evaluate the sensitivity to discover Z' (distinction from the SM) we look at the cross section and asymmetry on the resonance and in addition, at the asymmetry before the resonance. We found, (Fig. 14), that the contribution of the asymmetry before the resonance is insignificant in that case.

In addition, to examine the Z^* discovery potential we look at the cross section and the asymmetry on the resonance and cross section before the resonance. From

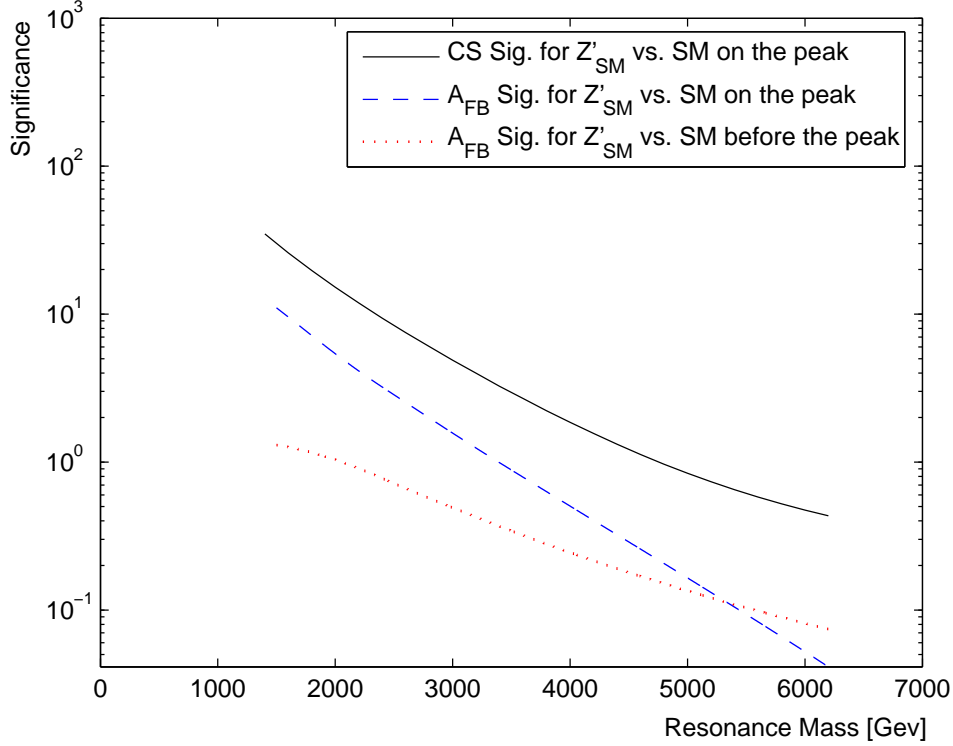


Figure 14: The significance for distinction between the Z'_{SM} and the SM model in the three methods: by cross section and forward-backward asymmetry measurements on the peak (solid and dash line) and forward-backward asymmetry before the peak (dotted line), corresponding to $\int L dt = 10\text{fb}^{-1}$

Fig. 15 one can see that there is a contribution from the measurement preceding the resonance but, it is smaller than the contribution of the measurement of cross section on the resonance. Therefore we can not predict the existence of the resonance measuring the cross section in low energies, since the measurement is always less significance than the measurement on the peak.

Our study shows that the only case in which we can predict the existence of the resonance from the measurement in lower energies, is when the luminosity is high enough however the resonance is beyond our mass reach. This can be relevant

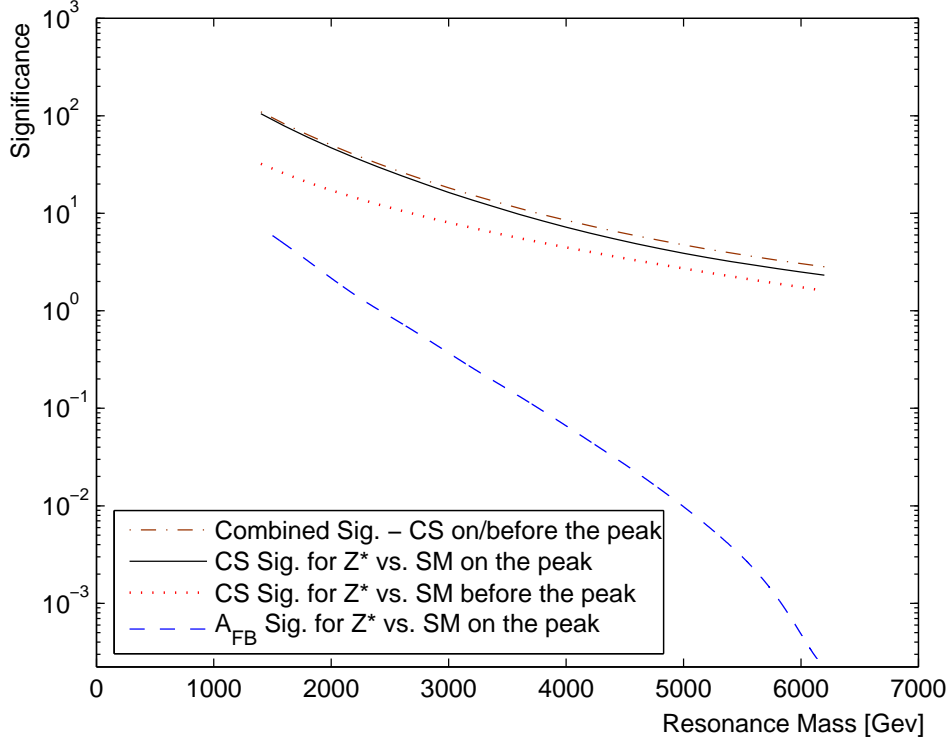


Figure 15: The significance for distinction between the Z^* and the SM model in the three methods: by cross section and forward-backward asymmetry measurements on the peak (solid and dash line) and cross section before the peak (dotted line), corresponding to $\int L dt = 10\text{fb}^{-1}$. In addition, the dash dotted line represents the combined significances of the cross section and the asymmetry on the peak

for several years of run of LHC or even for the SLHC. The effect is demonstrated in Fig. 16, where we show the cross section integration before the resonance with integrated luminosity of 500fb^{-1} . One can see that the measurement before the resonance is significant even at a mass of about 10TeV .

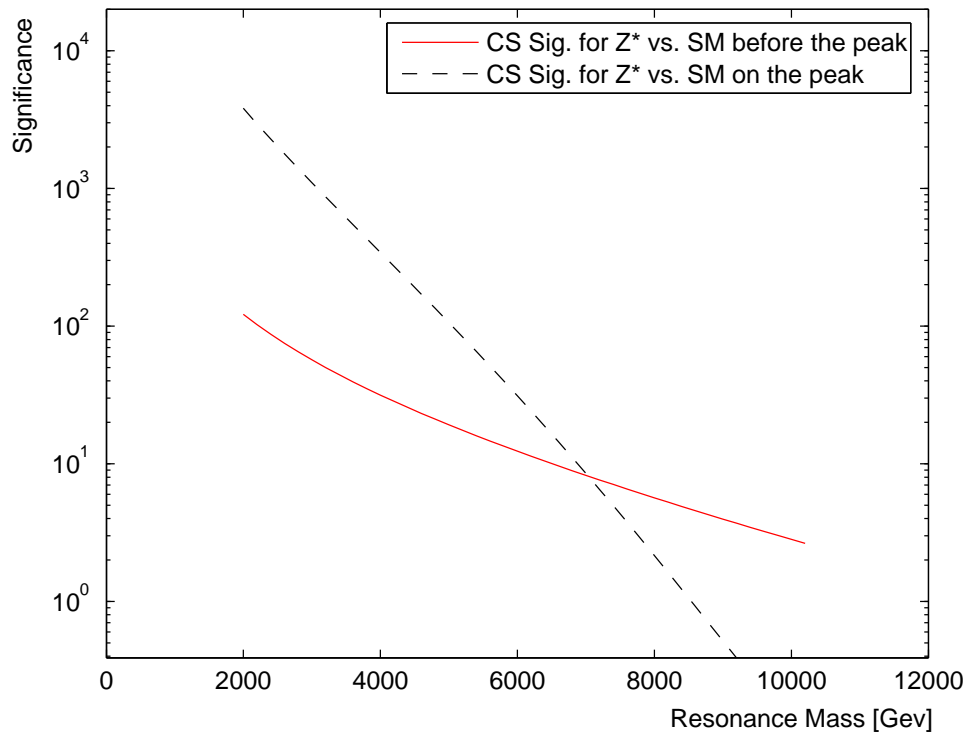


Figure 16: Z^* discovery significance using the cross section integration before the peak (solid) and on the peak (dashed), corresponding to $\int L dt = 500\text{fb}^{-1}$

5 Monte Carlo Generator

In order to get a better understanding of the experimental measurement we wanted to simulate the process. The simulation can be divided into three stages: (1) Proton interaction and generation of particles. (2) The hadronisation stage. (3) The interaction with the material in the detector.

For known physics one can use standard MC programs for the three stages. Programs like Pythia or, Herwig or others can simulate the event generation and the hadronisation process. The output of these programs can be processed with the detector simulation programs. Two of which are available for ATLAS (ATLfast - for fast but less detailed simulation and Full Geant4 based code which simulates the ATLAS detector in details.

Several New Physics process are available as well. One can use Pythia for generation of Z' . The code even allows you to choose various parameters set for its couplings. However in order to study the KK excitations of the Z boson we need to take care of its generation ourselves and let Pythia continue with the hadronisation stage.

In the following we describe our code for the simulation of the KK excitations. We created a large sample of simulated $pp \rightarrow l^+l^-X$ events. For each of them we were required to calculate the invariant mass of the di-lepton system and their angular distribution.

The code uses random number generator which provides us with numbers uniformly distributed. Our program transforms the numbers to follow the distributions predicted by the analytic calculations of the simulated process.

5.1 Invariant Mass Distribution

To obtain the correct mass distribution, we need to reproduce the neutral Drell-Yan process. After angular integration of Eq.(8), we get the following cross section:

$$\sigma(q\bar{q} \rightarrow \ell^- \ell^+) = \frac{\pi\alpha^2}{3M^2} \sum_{\lambda, \lambda'=\pm 1} \left| (\mathcal{A}^\gamma + \mathcal{A}_{\lambda, \lambda'}^Z + \mathcal{A}_{\lambda, \lambda'}^{\text{NP}}) \right|^2 \quad (29)$$

Therefore Eq.(7) gets the form:

$$\frac{d\sigma(pp \rightarrow \ell^- \ell^+ X)}{dM} = \frac{4}{3M} \sum_{q=d,u,s,c} \sigma(q\bar{q} \rightarrow \ell^- \ell^+) \cdot \int dy x_1 f_q(x_1, M^2) x_2 f_{\bar{q}}(x_2, M^2) \quad (30)$$

where y is the rapidity of the di-lepton system. In order to generate the events with the right M^2 distribution we need to define an approximate function, $\Phi(M^2)$, which will fulfill the condition:

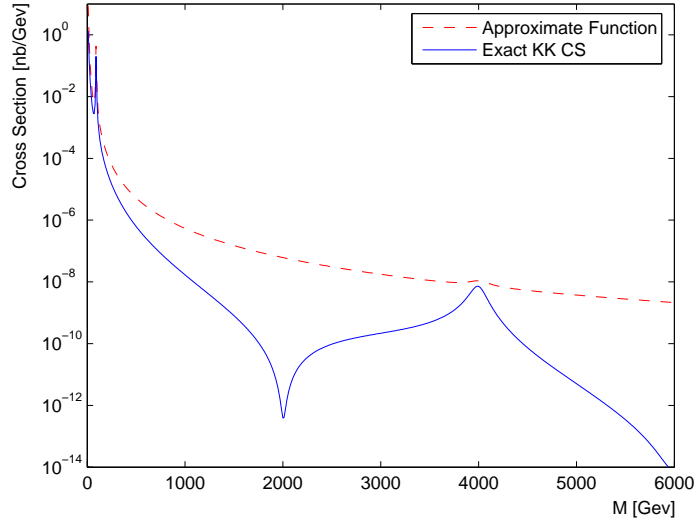


Figure 17: Exact KK cross section (solid) and the approximate function (dash)

$$\Phi(M^2) > \frac{d\sigma(pp \rightarrow l^- l^+ X)}{dM} \quad (31)$$

for all M^2 . The intuitive function used is:

$$\Phi(s) = \frac{A}{s^k} + \frac{B}{(s - M_{Z_0}^2)^2 + \Gamma_{Z_0}^2 M_{Z_0}^2} + \frac{C}{(s - M_{Z_{NP}}^2)^2 + \Gamma_{Z_{NP}}^2 M_{Z_{NP}}^2} \quad (32)$$

where $s = M^2$ and A, B, C and k are chosen to ensure the conditions Eq.(31), (Fig.17). The three terms in the approximate function correspond to the photon ($\Phi_1(s)$), the Z_0 boson ($\Phi_2(s)$) and the new physics resonance ($\Phi_3(s)$). In order to generate the variable s following the cross section distribution, we define the following:

$$I_i = \int_{s_{min}}^{s_{max}} \Phi_i(x) dx \quad (33)$$

$$F_i(s) = \frac{1}{I_i} \int_{s_{min}}^s \Phi_i(x) dx \quad (34)$$

were the $s_{min} = 10^2 \text{GeV}^2$ and $s_{max} = 14000^2 \text{GeV}^2$ (14 TeV is the maximum allowed energy at LHC). The functions $F_i(s)$ have a flat random distribution between 0 and 1, so they can be easily generated. Using $s(F_i)$ we get the s variable with Φ_i distribution. Each $\Phi_i(s)$ contributes to the total s distribution, proportional to it's weight - $\frac{I_i}{I_1+I_2+I_3}$. The rejection method is used to transform the distribution from the approximate expression given by Eq. (32) to the precise one, Eq.(30). To get s with the designed cross section distribution we use the conditions specified in Eq.(31). With additional random number, $n_{CS} \in [0, 1]$, we decide to keep the s if $n_{CS} \leq \frac{\sigma(s)}{\Phi(s)}$ were $\sigma(s) \equiv \frac{d^2\sigma(pp \rightarrow \ell^- \ell^+ X)}{dM d}$ (Eq.30).

In order to properly calculate the $\frac{d\sigma(pp \rightarrow \ell^- \ell^+ X)}{dM}$ for given s , we need to generate the rapidity, $y \in [0.5 \ln \left(\frac{s}{s_{max}} \right), -0.5 \ln \left(\frac{s}{s_{max}} \right)]$ which is required for x_1 and x_2 calculation.

$$x_1 = \left(\frac{s}{s_{max}} \right)^{\frac{1}{2}} e^y, \quad x_2 = \left(\frac{s}{s_{max}} \right)^{\frac{1}{2}} e^{-y} \quad (35)$$

A comparison between the theoretical cross section and the generated sample is shown in Fig.18

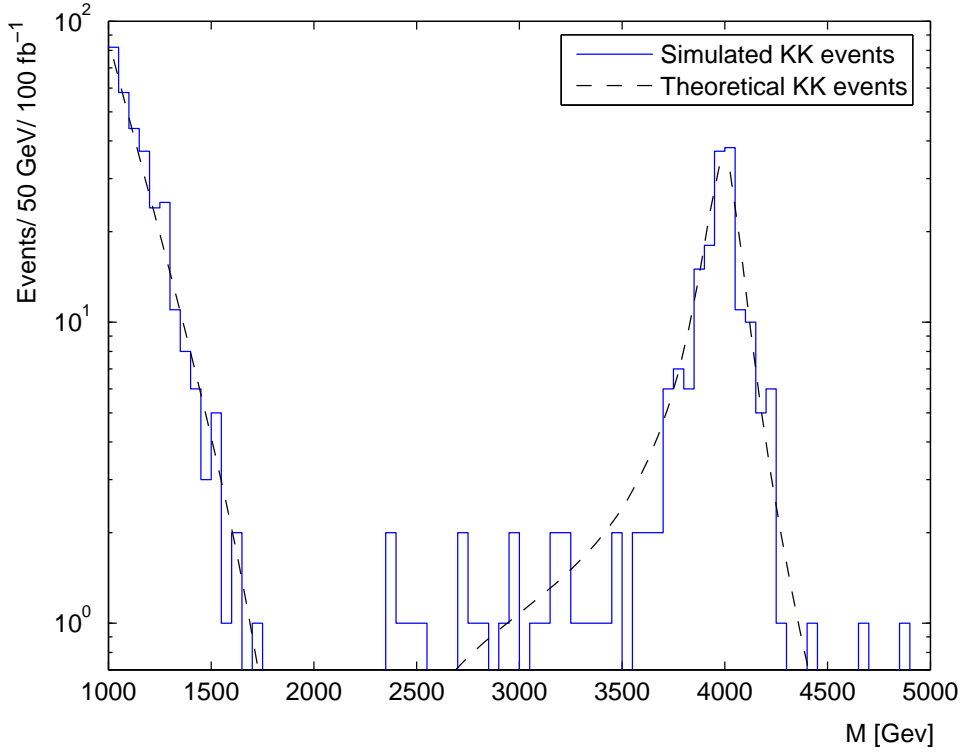


Figure 18: Simulated (solid) and theoretical (dash) mass distribution corresponding to $\int L dt = 100\text{fb}^{-1}$

5.2 Forward-Backward Asymmetry

The forward-backward asymmetry can be measured at the LHC only with respect to the boost direction. However in the simulation we control the process and therefore, the quark direction is known at the generation level.

The asymmetry calculation of the events is the second step in our MC generation process. This is done following the derivation of the s and the rapidity, y , of the event. It starts by selecting the $q\bar{q}$ pair which will physically interact out of the valence and sea quarks of the colliding protons. We assume four possible pair's: $u\bar{u}$, $d\bar{d}$, $s\bar{s}$ or $c\bar{c}$. In order to pick the specific pair, we use the PDF's (Fig. 19). For a given s we integrate the PDF expression for each pair. The probability to pick a

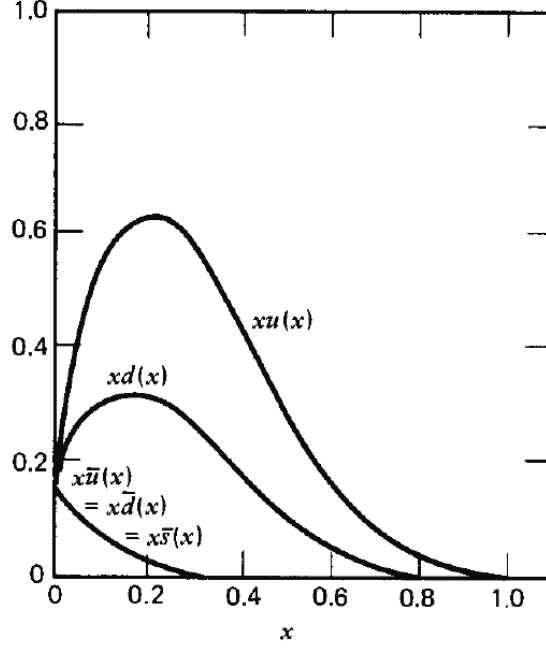


Figure 19: Parton Distribution Function - The fraction of the proton momentum carried by the different quarks.

specific $q\bar{q}$ from the proton is given by:

$$P_{q\bar{q}} = \frac{\int f_q(x_1) f_{\bar{q}}(x_2) dy}{\sum_i \int f_{q_i}(x_1) f_{\bar{q}_i}(x_2) dy} \quad (36)$$

Using a random number, $n_{q\bar{q}} \in [0, 1]$ we pick the pair of quarks corresponding to their expected fraction.

Usually, the quark will be more energetic than the anti-quark, that means that in general, the quark will have the larger x between x_1 and x_2 . In order to assure that the relations between the momentum of the generated q and \bar{q} follow the PDF expectation we do the following. We defined the probability to find quark with x_1 and anti-quark with x_2 by:

$$P_{qx_1} = \frac{f_q(x_1) f_{\bar{q}}(x_2)}{f_q(x_1) f_{\bar{q}}(x_2) + f_q(x_2) f_{\bar{q}}(x_1)} \quad (37)$$

In the $q = u$ and $q = d$ case - If $x_1 > x_2$ than $P_{qx_1} > P_{qx_2}$. So, by drawing a random number $n_x \in [0, 1]$, we will usually attribute the x_1 to the valence quark. For the s

and c quarks, the probability of the quark to have x larger than antiquark is equal. since they both come from the sea.

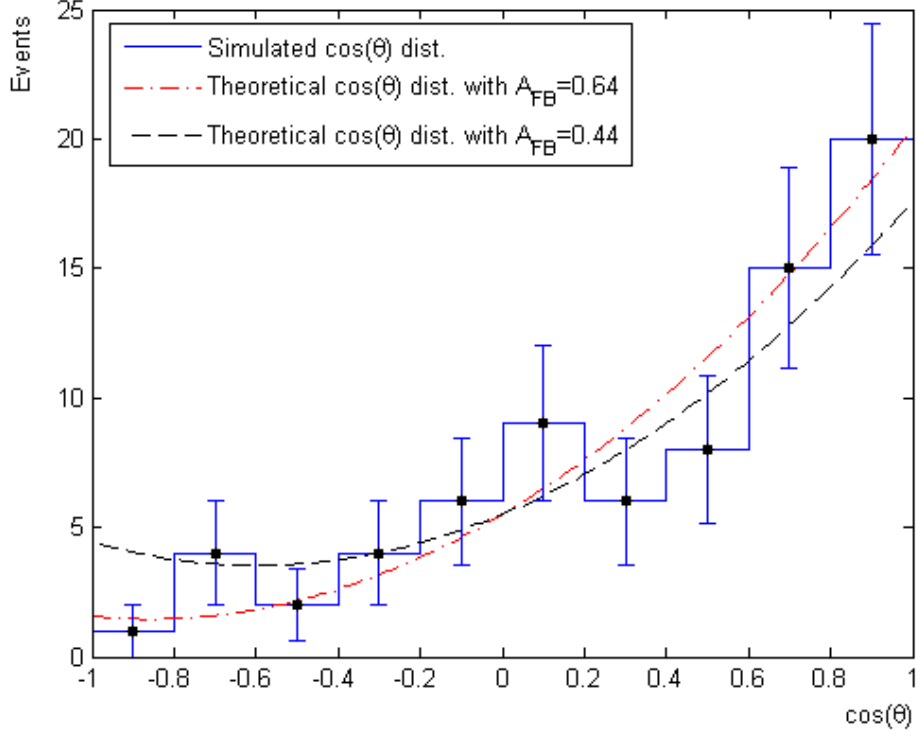


Figure 20: Simulated (solid) and theoretical (dash and dash dotted) $\cos(\theta)$ distribution corresponding to $\int L dt = 100\text{fb}^{-1}$. The band between the dashed and the dashed dotted lines represents the expected angular distribution with one standard deviation around the input ($A_{FB} = 0.54 \pm 0.1$) forward-backward asymmetry.

After determining the $q\bar{q}$ type and their energy's we need to calculate the coefficient of $\cos\theta^*$ in the forward-backward asymmetry equation,

$$f(\theta) = 1 + \cos(\theta)^2 + \frac{8}{3}A_{FB}\cos(\theta) \quad (38)$$

Using the Eq.(19) and (20) we get:

$$A_{FB} = \frac{3}{8} \frac{2B}{A} \quad (39)$$

We use the rejection method to generate $\cos(\theta)$ of the event. We start with choosing the $\cos(\theta) \in [0, 1]$ with uniform probability distribution and random number $n_{cos} \in$

$[0, 4]$ because the $f(\theta)$ function is bounded above by 4. The n_{cos} help us to decide whether we accept the $cos(\theta)$ or reject it. If the number is smaller than the $f(\theta)$ function, we accept the $cos(\theta)$. This procedure guarantees that we get the angular distribution of the events according to Eq. (38).

Fig. (20) demonstrates how the angular distribution of the generated events follow the required distribution.

6 Summary and Conclusions

We study the neutral Drell-Yan process $pp \rightarrow l^+l^- X$ in proton collisions at the LHC energy. We look for potential signature of deviation from the SM. Two possible deviations were considered: Based on KK excitations of $SU(2)$ and $U(1)$ gauge fields in the 5^{th} dimension while the matter fermions and $SU(3)$ gauge are localized in the 3d brane, we have modified the cross section of the Drell-Yan process, by adding new amplitudes for Z^* and γ^* . In addition, instead of KK excitations, we may assume the existence of an extra heavy boson coming from breaking of the E_6 group. In that case, the amplitude will be modified by a Z' contribution.

The different deviations introduced by these two models manifest themselves in the cross section search and forward-backward asymmetry: (1) The cross section with KK has a larger resonance enhancement compared with the Z' resonance and has a trough part before the resonance, due to the interference with the γ^* . (2) The forward-backward asymmetry of the Z' differs significantly from the SM behavior while the asymmetry of KK is similar to the SM one.

The main questions we have tried to answer in the current study were: The LHC sensitivity for discovering the KK excitations in the TeV scale and, if discovered, how to distinguish between KK and Z' models.

In order to estimate the possibility of discovering KK excitations or Z' by directly observing the resonance, we have studied the contribution of new physics signal added to the SM. We calculated the cross section upper limits and compared them with the expectations from the KK and various Z' models. We derive the upper limits of resonance masses which can be discovered or excluded at the LHC with $\int L dt = 10\text{fb}^{-1}$. We calculated the significance of the difference between the cross section distribution and forward-backward asymmetry for the KK, the Z' and the SM. We saw that the deviation in the cross section distribution is much more

pronounced than the forward-backward asymmetry.

In the second case, when the resonance is beyond our reach, we investigated the possibility to search for KK excitations by studying the cross section distribution while the Z' models are searched in the asymmetry distribution. We demonstrated that the deviation of the forward-backward asymmetry expected by the Z' below the resonance is not large enough to be detected. The best way to discover either the Z' or the KK signal would be from measurements on the peak. Nevertheless, the cross section distribution below the peak can improve the significance of the measurement in case of KK discovery or elimination. We saw that the only case in which we can predict the existence of the resonance from the measurement in lower energies, is when the luminosity is high enough however the resonance is beyond our mass reach. This can be relevant for several years of LHC or even the SLHC.

Along the analysis we assume that the differences from the SM predictions result only from the specific models discussed above. The study takes into account detector geometrical and resolution acceptance effects in a very crude way. We can improve on that, by taking simulated events through a realistic simulation model of one of the LHC detectors. Moreover, we did not take into account the "look elsewhere effect" when we calculated the 5σ (discovery) limit. This effect is expected to enhance the probability for background statistical fluctuation to reach a 5σ significance, by the value of the mass range divided by the resonance width. However, a more detailed study is needed to get a better estimation of this factor to determine the 5σ upper limit

To verify our conclusion, obtained by analytical calculations, we created a simulation program which generated simulated events following the same scheme. The results of the simulation agree well with our theoretical and numerical calculations. The next thing we plan to do is to combine the generator to a standard simulation code like Herwig or Pythia for the hadronisation stage and then let the generated

events go through realistic simulation of ATLAS and then use these events to repeat the calculations done in this work.

A Appendix - Kaluza-Klein Theory

Kaluza-Klein (KK) theory was based on Einstein's general relativity with additional, fifth dimension (Theodor Kaluza, 1921). The only reason to add an extra dimension was to derive both Einstein's general relativity and Maxwell's electromagnetic formulas from a single field. Because there was no empirical evidence for existence of the extra dimension, the single field variable had to depend only on the four space-time coordinates. This mean that all derivatives of the metric, with respect to the fifth coordinate, became zero ("cylinder condition").

In order to repeat Kaluza's steps, we will start with Einstein equation in five dimensions with the assumption that the five-dimensional space are empty, so there are no five dimensional energy-momentum tensor. The matter in four dimensions coming from geometric property's of high dimensional space-time. The equations is:

$$\hat{R}_{AB} - \frac{1}{2}\hat{g}_{AB}\hat{R} = 0 \quad (40)$$

Where the \hat{R}_{AB} and $\hat{R} = \hat{g}^{AB}\hat{R}_{AB}$ are the Ricci tensor and Ricci scalar respectively, \hat{g}_{AB} is the five-dimensional metric tensor and the capital Latin indices A and B run over 0, 1, 2, 3, 4. The new Christoffel symbols look like the symbols used in general relativity except that the indices run over five coordinates. The five-dimensional Christoffel symbols and Ricci tensor are defined by:

$$\hat{\Gamma}_{AB}^C = \frac{1}{2}\hat{g}^{CD}(\partial_A\hat{g}_{DB} + \partial_B\hat{g}_{DA} - \partial_D\hat{g}_{AB}) \quad (41)$$

$$\hat{R}_{AB} = \partial_C\hat{\Gamma}_{AB}^C - \partial_B\hat{\Gamma}_{AC}^C + \hat{\Gamma}_{AB}^C\hat{\Gamma}_{CD}^D - \hat{\Gamma}_{AD}^C\hat{\Gamma}_{BC}^D \quad (42)$$

Now, one can write the five-dimensional metric. Kaluza uses a 4 + 1 split where $g_{\alpha\beta}$ is the four-dimensional metric tensor, A_α the electromagnetic potential and ϕ is a scalar potential:

$$\hat{g}_{AB} = \begin{pmatrix} g_{\alpha\beta} + \kappa^2\phi^2 A_\alpha A_\beta & \kappa\phi^2 A_\alpha \\ \kappa\phi^2 A_\beta & \phi^2 \end{pmatrix} \quad (43)$$

Here we choose $c = 1$, $\hbar = 1$ and the signature of the four-dimensional metric is taken to be $(+, -, -, -)$. After we calculate the $\alpha\beta$, $\alpha 4$ and 44 components of the field in Eq.(40) using the metric(43), the definitions(41),(42) and the cylinder condition where we drop all derivatives with respect to the fifth coordinate, we find:

$$G_{\alpha\beta} = \frac{\kappa^2 \phi^2}{2} T_{\alpha\beta}^{EM} - \frac{1}{\phi} (\nabla_\alpha (\partial_\beta \phi) - g_{\alpha\beta} \square \phi) \quad (44)$$

$$\nabla^\alpha F_{\alpha\beta} = -3 \frac{\partial^\alpha \phi}{\phi} F_{\alpha\beta} \quad (45)$$

$$\square \phi = \frac{\kappa^2 \phi^3}{4} F_{\alpha\beta} F^{\alpha\beta} \quad (46)$$

where $T_{\alpha\beta}^{EM} \equiv \frac{1}{4} g_{\alpha\beta} F_{\gamma\delta} F^{\gamma\delta} - F_\alpha^\gamma F_{\beta\gamma}$ is the electromagnetic energy-momentum tensor, $G_{\alpha\beta}$ is the Einstein tensor, ∇_α is the covariant derivative such that the derivative of a vector is now given by $\nabla_\alpha V_\beta = \frac{\partial V_\beta}{\partial x^\alpha} - \Gamma_{\alpha\beta}^\gamma V_\gamma$, $\square \equiv g^{\alpha\beta} \nabla_\alpha \nabla_\beta$ is the wave operator and $F_{\alpha\beta}$ defined by $F_{\alpha\beta} \equiv \partial_\alpha A_\beta - \partial_\beta A_\alpha$.

To get the original Einstein and Maxwell equations we set the scalar field to be a constant (Kaluza set $\phi = 1$) and the scaling parameter $\kappa \equiv 4\sqrt{\pi G}$. In this case from Eq. (44) and (45) we get Einstein and Maxwell equation respectively:

$$G_{\alpha\beta} = 8\pi G \phi^2 T_{\alpha\beta}^{EM} \quad (47)$$

$$\nabla^\alpha F_{\alpha\beta} = 0 \quad (48)$$

If we don't set the scalar field to be a constant we end up with a Brans-Dicke type scalar field theory besides the electromagnetic one [23].

Nowadays, the derivation is usually repeated in variational language. Instead of starting with Eq. (40) we may use the five-dimensional action:

$$S = -\frac{1}{16\pi\hat{G}} \int d^4x dy \sqrt{-\hat{g}} \hat{R} \quad (49)$$

Using the metric (43), the definitions (41,42) and the cylinder condition, one can rewrite the action (49) in the following way:

$$S = - \int d^4x \sqrt{-g} \phi \left(\frac{R}{16\pi G} + \frac{1}{4} \phi^2 F_{\alpha\beta} F^{\alpha\beta} + \frac{2}{3k^2} \frac{\partial^\alpha \phi \partial_\alpha \phi}{\phi^2} \right) \quad (50)$$

where G is defined in terms of five-dimensional gravitational constant: $G \equiv \hat{G}/\int dy$. Once again, setting the scalar field to a constant we get the Einstein-Maxwell action for gravity and electromagnetic radiation. The third component is the action for a massless Klein-Gordon scalar field.

The extra factor of ϕ in (50) implies that, the gravitational part of the action will be in a canonical form if the scalar field will be constant throughout space-time. This, of course, is not a generally covariant procedure, so we can solve this by conformally rescaling the five-dimensional metric:

$$\hat{g}_{AB} \rightarrow \hat{g}'_{AB} = \Omega^2 \hat{g}_{AB} \quad (51)$$

where $\Omega^2 > 0$ is the conformal factor, a function of four coordinates only. Now if we make the following redefinition, $\phi^2 \rightarrow \phi$ and introducing the conformal factor $\Omega^2 = \phi^{-1/3}$, we get the rescaled five-dimensional metric:

$$\hat{g}'_{AB} = \phi^{-1/3} \begin{pmatrix} g_{\alpha\beta} + \kappa^2 \phi A_\alpha A_\beta & \kappa \phi A_\alpha \\ \kappa \phi A_\beta & \phi \end{pmatrix} \quad (52)$$

Eq. (50) becomes now to the conformal rescaled action:

$$S' = - \int d^4x \sqrt{-g'} \left(\frac{R'}{16\pi G} + \frac{1}{4} \phi F'_{\alpha\beta} F'^{\alpha\beta} + \frac{1}{6k^2} \frac{\partial'^\alpha \phi \partial'_\alpha \phi}{\phi^2} \right) \quad (53)$$

where $\partial'^\alpha \phi = g'^{\alpha\beta} \partial_\beta \phi$. Now we do not have the extra factor of ϕ and the gravitational part of the action has the conventional form.

So, we are starting with five-dimensional, empty, space-time and getting the four-dimensional matter, purely from the geometry of the first one. To explain why we don't see the fifth dimension and where from do we get the cylinder conditions, Oscar Klein assumed in 1926 that the fifth dimension has a circular topology (S^1) and very small scale. Klein suggested that there is a circle at each point in four-dimensional space-time. Because of the periodicity ($f(x, y) = f(x, y + 2\pi r)$), we can expand the fields:

$$g_{\alpha\beta}(x, y) = \sum_{n=-\infty}^{n=\infty} g_{\alpha\beta}^{(n)}(x) e^{iny/r} \quad (54)$$

$$A_\alpha(x, y) = \sum_{n=-\infty}^{n=\infty} A_\alpha^{(n)}(x) e^{iny/r} \quad (55)$$

$$\phi(x, y) = \sum_{n=-\infty}^{n=\infty} \phi^{(n)}(x) e^{iny/r} \quad (56)$$

so the Kaluza-Klein theory describes an infinite number of four-dimensional fields. From quantum theory, the Fourier modes have a momentum of the order $\frac{|n|}{r}$, where r is the radius of the fifth dimension. If we assume that the radius is extremely small, it will be clear why it is so hard to test experimentally the existence of the fifth dimension. The momentum of all modes, except for $n = 0$, will be larger than the experimental energy range. The $n = 0$ modes, which are observables, are independent of y , as required in the Kaluza's theory.

Now we want to derive the masses from the Kaluza-Klein theory. As a simplest kind of matter let us look on massless five-dimensional scalar field $\hat{\varphi}(x, y)$. It's action would have a kinetic part only:

$$S_{\hat{\varphi}} = - \int d^4x dy \sqrt{-\hat{g}} \partial^A \hat{\varphi} \partial_A \hat{\varphi} \quad (57)$$

That field can also be expanded:

$$\hat{\varphi}(x, y) = \sum_{n=-\infty}^{n=\infty} \hat{\varphi}^{(n)}(x) e^{iny/r} \quad (58)$$

When this expansion is substituted into action (57) and the Eq. (52) is used, we receive the following:

$$S_{\hat{\varphi}} \sim - \sum_n \int d^4x \sqrt{-g} \left[\left(\partial^\alpha + \frac{in\kappa A^\alpha}{r} \right) \hat{\varphi}^{(n)} \left(\partial_\alpha + \frac{in\kappa A_\alpha}{r} \right) \hat{\varphi}^{(n)} - \frac{n^2}{\phi r^2} \hat{\varphi}^{(n)2} \right] \quad (59)$$

The masses of the scalar modes are given by the square root of the coefficient of the $\hat{\varphi}^{(n)2}$ term:

$$m_n = \frac{|n|}{r\sqrt{\phi}} \quad (60)$$

Acknowledgements

I would like to thank my supervisors, Prof. Erez Etzion and Prof. Yaron Oz, for introducing me to the Kaluza-Klein theory and guiding me through this research, looking for new physics beyond the standard model at the LHC.

I would also like to express my deep appreciation to Dr. Gideon Bella for his dedicated guidance, support, endless knowledge and experience.

I am grateful for the friendship of all those people with whom I have spent the last two and a half years, in particular (and in strictly alphabetical order!): Gideon Alexander, Nir Amram, Meny Ben Moshe, Yan Benhammou, Hadas Frostig, Avi Gershon, Jonatan Ginzburg, Nir Guttman, Noam Hod, Yair Mahalalel, Erez Reinherz-Aronis, Abner Soffer.

Finally, I thank my family and friends for their continuing and unfailing support and encouragement in everything I do, without which none of this would be possible. I would specially like to thank my life partner and best friend, Diana, for her's support and love.

List of Figures

| | | |
|---|--|----|
| 1 | Neutral Drell-Yan process $pp \rightarrow l^+ l^- X$ with additional gauge fields. | 3 |
| 2 | The string theory describes our Universe using extra dimensions. Beside the three known spatial dimensions (single blue line) there are parallel extra dimensions - p -brane (green plane) where endpoints of open strings are confined and transverse dimensions (yellow space) where only gravity can propagate (closed string) [2]. | 6 |
| 3 | Overview of the accelerator complex at CERN. | 11 |
| 4 | Proton-proton cross section of the different process as a function of the center-of-mass energy. | 12 |
| 5 | The ATLAS detector, with the main components highlighted. | 13 |
| 6 | Momentum resolution for muons reconstructed in the Muon Spectrometer as a function of transverse momentum averaged over $ \eta < 1.5$ (left plot) and averaged over $ \eta > 1.5$ (right plot). | 16 |
| 7 | Efficiency as a function of invariant mass. For each energy we calculate the numbers of expected events with and without the cuts on rapidity and p_T . The plot represents the ratio of the di-lepton mass distributions with and without those cuts | 18 |
| 8 | Di-lepton mass distribution before the cuts. Dashed curve shows the expected SM distribution with peak of the Z^0 is seen at 90 GeV. The solid curve shows the KK excitations with the first excited state mass set to 4TeV, and the dash dot curve - the Z' | 21 |

| | | |
|----|--|----|
| 9 | Expected visible cross sections for the various Z' models and for the KK model compared with the cross section upper limit of 2σ and 5σ . The crossing points corresponds to the upper limits of the resonance mass which can be excluded/discovered at the LHC corresponding to integrated luminosity of 10fb^{-1} | 24 |
| 10 | Expected visible cross sections for the various Z' models and for the KK model compared with the cross section upper limit of 2σ and 5σ . The crossing points corresponds to the upper limits of the resonance mass which can be excluded/discovered at the LHC corresponding to integrated luminosity of 100fb^{-1} | 25 |
| 11 | Forward-Backward Asymmetry for the KK excitations and the Z'_{SM} , with and without the cuts: $P_T > 10 \text{ GeV}$, $ y < 2.5$. The asymmetry was calculated with respect to the boost direction. | 29 |
| 12 | Upper plot: forward-backward asymmetry of the KK resonance with 3σ errors (painted area), asymmetry of the Z'_{SM} resonance without the errors (solid line) and asymmetry of the Z'_χ resonance without the errors (dashed-dotted line). Bottom plot: forward-backward asymmetry of the Z'_{SM} resonance with 3σ errors (painted area), asymmetry of the KK resonance without the errors (solid line) and asymmetry of the Z'_χ resonance without the errors (dashed-dotted line). | 30 |
| 13 | The significance for distinction between the Z'_{SM} and the KK model by cross section and forward-backward asymmetry measurements on the peak, corresponding to $\int Ldt = 10\text{fb}^{-1}$ | 32 |

| | | |
|----|---|----|
| 14 | The significance for distinction between the Z'_{SM} and the SM model in the three methods: by cross section and forward-backward asymmetry measurements on the peak (solid and dash line) and forward-backward asymmetry before the peak (dotted line), corresponding to $\int Ldt = 10\text{fb}^{-1}$ | 34 |
| 15 | The significance for distinction between the Z^* and the SM model in the three methods: by cross section and forward-backward asymmetry measurements on the peak (solid and dash line) and cross section before the peak (dotted line), corresponding to $\int Ldt = 10\text{fb}^{-1}$. In addition, the dash dotted line represents the combined significances of the cross section and the asymmetry on the peak | 35 |
| 16 | Z^* discovery significance using the cross section integration before the peak (solid) and on the peak (dashed), corresponding to $\int Ldt = 500\text{fb}^{-1}$ | 36 |
| 17 | Exact KK cross section (solid) and the approximate function (dash) . . . | 38 |
| 18 | Simulated (solid) and theoretical (dash) mass distribution corresponding to $\int Ldt = 100\text{fb}^{-1}$ | 40 |
| 19 | Parton Distribution Function - The fraction of the proton momentum carried by the different quarks. | 41 |
| 20 | Simulated (solid) and theoretical (dash and dash dotted) $\cos(\theta)$ distribution corresponding to $\int Ldt = 100\text{fb}^{-1}$. The band between the dashed and the dashed dotted lines represents the expected angular distribution with one standard deviation around the input ($A_{FB} = 0.54 \pm 0.1$) forward-backward asymmetry. | 42 |

List of Tables

| | | |
|---|--|----|
| 1 | Couplings of Z' models coming from breaking the E_6 group. | 9 |
| 2 | High energy collider parameters for TEVATRON and LHC [13]. | 10 |
| 3 | Mass limits for integrated luminosity of 10fb^{-1} | 25 |
| 4 | Mass limits for integrated luminosity of 100fb^{-1} | 26 |

References

- [1] L. Randall, Phys. Today (2007), "The case for extra dimensions".
- [2] I. Antoniadis, arXiv:hep-ph/0512182v1.
- [3] N. Arkani-Hamed, S. Dimopoulos, G. Dvali, arXiv:hep-ph/9803315v1.
- [4] L. Randall, R. Sundrum, arXiv:hep-th/9905221.
- [5] C. Csaki, C. Grojean, J. Hubisz, Y. Shirman, and J. Terning, arXiv:hep-ph/0310355; C. Csaki, C. Grojean, L. Pilo and J. Terning, arXiv:hep-ph/0308038; C. Csaki, C. Grojean, h. Murayama, L. Pilo and J. Terning, arXiv:hep-ph/0305237; Y. Nomura, arXiv:hep-ph/0309189; E. H. Simmons, R. S. Chivukula, H. J. He, M. Kurachi, M. Tanabashi, arXiv:hep-ph/0606019v1.
- [6] P. Binetruy, C. Deffayet and D. Langlois, arXiv:hep-ph/9905012; T. Appelquist, H. C. Cheng and B. A. Dobrescu, arXiv:hep-ph/0012100; H. C. Cheng K. T. Matchev and M. Schmaltz, arXiv:hep-ph/0205314.
- [7] S. Dimopoulos and G. Landsberg, arXiv:hep-ph/0106295; S. B. Giddings and S. Thomas, arXiv:hep-ph/0106219; S. B. Giddings and Vv. S. Rychkov, arXiv:hep-ph/0409131.
- [8] T. G. Rizzo, arXiv:hep-ph/9909232v4.
- [9] G. Azuelos, G. Polesello, Eur. Phys. J C 39, (2004).
- [10] M. Schafer, F. Ledroit, B. Trocme, ATL. PHYS. PUB. 2005, 010.
- [11] K. Hagiwara et al. (Particle Data Group), Phys. Rev. D66 (2002) 010001
- [12] F. Abe et al. (CDF coll), Phys. Rev. Lett. 79 (1997) 2192
- [13] K. Desler and D. A. Edwards (Particle Data Group), Accelerator Physics of Colliders.

- [14] CDF II, Phys. Rev. Let. PRL 99, 171802 (2007).
- [15] T. Sjöstrand, S. Mrenna and P. Skands, JHEP **05** (2006) 026.
- [16] J. Pumplin *et al.*, JHEP **0207** (2002) 012.
- [17] M.R. Whalley, D. Bourilkov and R.C. Group, arXiv:hep-ph/0508110v1.
- [18] P. Mathews, V. Ravindran and K. Sridhar, JHEP **10** (2005) 031.
- [19] A. Cafarella, C. Coriano and M. Guzzi, JHEP **08** (2007) 030.
- [20] C. Coriano, A.E. Faraggi and M. Guzzi, arXiv:0802.1792v2 [hep-ph].
- [21] L. Evans and P. Bryant (editors). LHC Machine. Journal of Instrumentation, 3(08):S08001, 2008.
- [22] The ATLAS Collaboration, CERN-OPEN-2008-020.
- [23] J. M. Overduim and P. S. Wesson, arXiv:gr-qc/9805018v1.